

U.O.V.S. BIBLIOTEK

University Free State



34300000407977

Universiteit Vrystaat

HIERDIE EKSEMPLAAR MAG ONDER
GEEN OMSTANDIGHED E UIT DIE
BIBLIOTEEK VERWYDER WORD NIE

**AN EVALUATION OF THE EFFECT OF SCATTER AND ATTENUATION
CORRECTION OF GAMMA PHOTONS ON THE RECONSTRUCTED
RADIONUCLIDE DISTRIBUTION OF THE INFERIOR MYOCARDIAL WALL
DURING SPECT IMAGING**

by

Nhlakanipho Mdletshe

This dissertation is submitted to meet the requirements for the degree Masters in Medical Science (M.Med Sc) in the Faculty of Health Sciences, Department of Medical Physics at the University of the Orange Free State.

November 2000

Supervisor: Prof A van Aswegen
Co-supervisor: Dr H du Raan

Universiteit van die
Oranje Vrystaat
BLOEMFONTEIN

21 MAY 2001

HOVS SAKEL BE I 1000

I declare that the dissertation which is hereby submitted for the degree Masters in
Medical Science (M.Med Sc) at the University of the Orange Free State is of my own
independent work and has not been handed in before for a degree at/ in another
University/ Faculty.

Bloemfontein

November 2000

_____

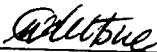
Nhlakanipho Mdletshe

TO WHOM IT MAY CONCERN

I hereby concede the copyright of this dissertation to the University of the Orange Free
State

Bloemfontein

November 2000



Nhlakanipho Mdletshe

Preface

Research is necessary for the development and improvement of our standard of living. Research success needs the contribution of different people. For this research I would like to thank Prof A van Aswegen for helping me to choose the topic of this study, his effort to help me with all the problems of the research and to check all the results on his tight schedule. Dr H du Raan was always there on the practical purpose, image analysis, programming and all the difficulties I met in this project. I would also like to thank Prof MG Lötter and the Medical Physics (UOFS) staff for the discussion of this project. I would also like to thank Prof DG van der Merwe for giving me time at the Johannesburg Hospital so that I could finish this project.

This project was done at the Nuclear Medicine department, Universitas Hospital. Prof AC Otto and the Nuclear Medicine staff were so good to give me the chance to do practical work in spite of the hectic clinical schedule.

Prof HC Swart on behalf of the NRF is thanked for the financial support. The support from my friends, colleagues and family encouraged me through this project. The encouragement from KT Hillie the Physics PhD student and friend was great. My mother, Patricia, my brothers, Muzi, Nduduzo and Bongani were always there when needed.

**AN EVALUATION OF THE EFFECT OF SCATTER AND ATTENUATION CORRECTION OF
GAMMA PHOTONS ON THE RECONSTRUCTED RADIONUCLIDE DISTRIBUTION OF THE
INFERIOR MYOCARDIAL WALL DURING SPECT IMAGING.**

INDEX

1. Introduction
2. Literature review
3. Phantom studies to evaluate reconstruction parameters for myocardial perfusion studies
4. Clinical evaluation of attenuation and scatter corrections in myocardial perfusion studies
5. Summary

CHAPTER 1

Introduction

The coronary arteries nourish the myocardial muscles with oxygenated blood. These coronary arteries can be obstructed by a thrombus that causes the myocardial muscle to receive inadequate blood supply. Coronary artery disease (CAD) can result. Various methods have been used for the diagnosis of CAD. Nuclear medicine studies such as myocardial perfusion imaging can be used to evaluate the blood supply to the myocardial muscle and contribute to the diagnosis of this disease.

Nuclear Medicine images are degraded mainly due to attenuation and Compton scatter of the emitted photons (in this literature attenuation often refers to absorption and scatter. In this dissertation however attenuation is regarded as absorption only and scatter is treated separately). Single photon emission computed tomography (SPECT) is an imaging technique used in nuclear medicine for tomographic *in vivo* evaluation of the distribution of a radiopharmaceutical in the patient. Myocardial perfusion studies have been performed using either ^{201}Tl (energy 72keV and half-life 72.1 hours) (Gallowitsch et al., 1998 and Chouraqui et al., 1998) or a $^{99\text{m}}\text{Tc}$ labelled agent. ^{201}Tl has the advantage of a better extraction fraction and a linear relation with myocardial blood flow while the $^{99\text{m}}\text{Tc}$ labelled agent with the higher energy (140keV) results in lower tissue attenuation, and therefore a higher count rate. The shorter physical (6.02hours) and biological half-life of the latter limit the radiation dose to the patient (English et al., 1993).

Quantification is the ultimate challenge in clinical nuclear medicine for both diagnostic and therapeutic purposes. In SPECT, photon attenuation and the contribution from scattered photons impose important limitations with regards to the quantification of activity within specific regions (Almquist et al., 1990). For the myocardial perfusion studies, a major problem associated with the accurate detection of these photons is attenuation and scatter of photons originating in the inferior myocardial wall of the left ventricle. This causes a decreased regional radionuclide uptake in the clinical perfusion studies that can be interpreted as an insufficient blood supply to that region, thus leading to a possibility of a false positive diagnosis with severe consequences to the patient. The application of attenuation and scatter correction can improve the diagnostic accuracy and lead to better interpretation of clinical studies.

Other factors, apart from the attenuation and scatter of photons, affect the quantification of the radionuclide distribution in a scattering medium e.g. the detector response of the imaging equipment, patient motion (Cooper et al., 1992) and the algorithm used for reconstructing the data. It was found that the effect of detector response correction was generally small according to phantom studies by Naudé (1998). Furthermore, patient motion was be minimised by making the acquisition time as short as possible.

The most commonly used reconstruction algorithm in SPECT is based on filtered back-projection (FBP). FBP can be easily applied and provides accurate reconstruction for ideal SPECT data not degraded by physical factors such as attenuation and scatter of photons. However, with FBP the reconstructed image will

be limited in terms of accurate quantification, spatial resolution and contrast. Image artefacts and distortion may also result in streaking artefacts that are created using FBP (Tsui et al, 1994). Iterative reconstruction algorithms can account for non-uniform attenuation and provide more accurate quantification results (Chronoboy et al., 1990). The choice of the iterative algorithm is important. A widely used technique is the maximum likelihood expectation maximization algorithm (MLEM). The MLEM method provides accurate results (Miller et al., 1992) but converges slowly (Galt et al, 1999). The slow converging characteristics yield a greater control over image noise (Tsui et al., 1989). An accelerated iterative reconstruction algorithm, the ordered subset expectation maximization (OSEM) algorithm, based on the expectation maximization technique was introduced by Hudson and Larkin, 1994. This approach performs an ordering of the projection data into subsets. The subsets are used in the iterative steps of the reconstruction to greatly speed up the reconstruction and are therefore clinically useful.

Compensation for attenuation in SPECT imaging is difficult to attain since the source is of an unknown distribution and is located in a medium of unknown composition. The most common methods for attenuation compensation used in commercial systems until recently are based on the work by Chang (1978) and Sorenson (1984). These methods assume that the attenuation within the body is uniform. However an assumption of uniform attenuation medium in the thorax region can result in enormous errors. If a map of the attenuation coefficients can be obtained from the body being studied, it can be applied to the SPECT data during reconstruction to attain the necessary attenuation correction. The attenuation co-efficient can be

obtained by acquiring transmission images from the body using an external radioactive source (Bailey et al., 1987).

Another important but different problem for quantification in SPECT is scatter correction. The effects of scattered photons on SPECT imaging include reduced image contrast and inaccurate quantification measurement (Tsui et al., 1994). The scatter compensation methods for SPECT require the estimation of the number of scattered photons in each pixel of the image. This is complex because the scatter components of the image depend on the energy of the photon, the energy window used, the composition and location of the source and scattering medium (Frey and Tsui, 1994). The triple energy window technique described by Ogawa (1991) corrects for scatter using an energy window selected in the scatter region of the energy spectrum. This technique requires no pre-calibration, and can be used in clinical practise. This correction technique was implemented during this study to compensate for scattered photons.

The aim of this study was firstly to evaluate the selection of appropriate parameters for the iterative reconstruction algorithm. This was done in phantom studies and the influence of the number of iterations and subsets on the resolution and noise of the images was investigated. Secondly, the effect of scatter and attenuation corrections in the final diagnosis of myocardial perfusion studies was evaluated. Myocardial perfusion studies were performed on three groups of subjects, namely normal male volunteers, normal female volunteers and a group of patients with proven inferior myocardial defect.

Reference

- Almquist H, Palmer J, Ljungberg M, Wollmer P, Strand S-E, Jonson B (1990). Quantitative SPECT by attenuation correction of the projection set using transmission data: Evaluation of a method. *Eur J Nucl Med*; 16: pp587 – 594.
- Bailey DL, Hutton BF, Walker PJ (1987). Improved SPECT using simultaneous emission and transmission tomography. *J Nucl Med*; 28: pp844 – 851.
- Chang LT (1978). A method for attenuation correction in radionuclide computed tomography. *IEEE Trans Nucl Sci*; NS-25: pp638 – 643.
- Chornoboy ES, Chen CJ, Miller MI, Miller TR, Snyder DL (1990). An evaluation of maximum likelihood reconstruction for SPECT. *IEEE Trans Med Imag*; 9: pp99–110.
- Chouraqui P, Livschitz S, Sharir T, Wainer N, Wilk M, Moalem I, Baron J (1998). Evaluation of an attenuation correction on method for thallium-201 myocardial perfusion tomographic imaging of patients with a low likelihood of coronary artery disease. *J Nucl Card*; 5:369-377.
- Cooper JA, Neumann PH, McCandless BK (1992). Effect of patient motion on tomographic myocardial perfusion imaging. *J Nucl Med*; 33:p1566 – 1571.
- English CA, English R J, Giering LP, Manspeaker H, Murphy JH, Wise PA (1993). *Introduction to nuclear cardiology 3rd ed*, Du Pont Pharma; Massachusetts; USA: pp173 - 198
- Frey EC and Tsui BMW (1994). Modelling the scatter response function in inhomogeneous scattering media for SPECT. *IEEE Trans Nucl Sci*; 41: pp1585 – 1593.
- Gallowitsch JH, Sykora J, Mikosch P, Kresnik E, Unterweger O, Molnar M, Grimm G, Lind P (1998) Attenuation-corrected thallium-201 single-photon emission tomography using gadolinium line source: Clinical value and the impact of attenuation correction on the extent and severity of perfusion abnormalities. *J Nucl Med*; 25: pp220 – 228.
- Galt JR, Cullom SJ, Garcia EV (1999). Attenuation and scatter compensation in myocardial perfusion SPECT. *Seminars in nuclear medicine*; XXIX, pp204 – 220.
- Hudson HM and Larkin RS (1994). Accelerated image reconstruction using ordered subsets of projection data. *IEEE Trans Med Imag*; 20: pp100 – 108.
- Miller TR, Wallis JW (1992). Clinically important characteristics of maximum-likelihood reconstruction. *J Nucl Med*; 33: pp1678 – 1684.
- Naudé H (1998). Scatter and attenuation correction techniques for absolute quantification of radionuclide distributions with SPECT. *PhD Thesis*, UOVS, Bloemfontein.

Ogawa K, Harata Y, Ichihara T, Kubo A, Hashimoto S (1991). A practical method for position-dependent Compton-scatter correction in single photon emission CT. *IEEE Trans Med Imag*; 10: pp408 – 412.

Sorenson JA (1984). Quantitative measurement of radiation *in vivo* by whole body counting, in Hine GH, Sorenson JA (eds): *Instruments in nuclear medicine*, vol 2. New York, NY, Academic, pp 311-349.

Tsui BMW, Gullberg GT, Edgerton ER, Ballard JG, Perry JR, McCartney WH, Berg J (1989). Correction of nonuniform attenuation in cardiac SPECT imaging. *J Nucl Med*; 30: pp497 – 507.

Tsui BMW, Zhao X, Frey EC, McCartney WH (1994). Quantitative Single- Photon Emission Computed Tomography: Basic and clinical consideration. *Seminars in Nuclear medicine*; xxiv: pp38 – 65.

CHAPTER 2: LITERATURE REVIEW

2.1 Introduction.....	2.1
2.2 Attenuation compensation	2.7
2.2.1 Introduction.....	2.7
2.2.2 Conventional methods	2.7
2.2.3 Transmission-based attenuation correction.....	2.9
2.2.3.1 Selection of a radionuclide source for transmission imaging.....	2.15
2.2.3.2 Simultaneous or sequential data acquisition	2.17
2.2.4 Emission based attenuation correction.....	2.18
2.3 Scatter correction	2.21
2.3.1 The triple energy window scatter correction technique.....	2.24
2.4 Compensation of detector response function	2.27
2.5 Single Photon Emission Computed Tomography reconstruction algorithms	
.....	2.28
2.5.1 Introduction.....	2.28
2.5.2 Analytical reconstruction algorithms.....	2.30
2.5.2.1 The Back-projection reconstruction algorithms.....	2.30
2.5.2.2 Filtered Back-projection reconstruction algorithms.....	2.31
2.5.3 Iterative reconstruction algorithms	2.32
2.5.3.1 Iterative Filtered Back-Projection algorithms	2.33
2.5.3.2 Statistical reconstruction algorithms	2.33
2.5.3.2.2 Expectation maximisation algorithm	2.36
2.5.3.2.3 Statistical Background	2.36

2.5.3.2.4 Expectation Maximisation Reconstruction Algorithm.....	2.37
2.5.4 Accelerated iterative techniques.	2.40
2.5.4.1 Introduction	2.40
2.5.4.2 Ordered Subsets Expectation Maximisation Reconstruction algorithm	2.41
2.5.4.3 Selection of subsets and order of reconstruction.	2.42
2.5.5 Separable paraboloidal surrogate reconstruction.....	2.43
2.6 Discussion.....	2.44
References	2.46

2.1 Introduction

Single photon emission computed tomography (SPECT) has been established as an important tool in diagnostic nuclear medicine, especially in cardiac, brain and bone perfusion studies (Tsui et al., 1994a).

In cardiac perfusion studies, SPECT is used as a non-invasive method for management and diagnosis of patients with coronary artery disease (CAD). A major problem associated with accurate quantification in SPECT is the attenuation of photons from the organ of interest and the presence of photons scattered from surrounding organs. Attenuation is the most important degrading factor in SPECT. It limits the sensitivity (the ability to detect disease when it is present) and specificity (the ability to rule out disease when it is absent) of cardiac SPECT imaging by causing a variation in normal tracer distribution (Miles et al., 1999). This variation may be mistaken for a regional myocardial perfusion defect and therefore may result in a false positive diagnosis.

The most commonly described clinical effects of attenuation are image artefacts associated with breast and diaphragm attenuation in women and men respectively (DePeuy and Garcia, 1989; DePeuy 1994).

Breast attenuation artefacts commonly appear in the tomographic images as a regional decreased count density in the anterior and lateral myocardial walls of the left ventricle. Diaphragm attenuation artefacts are associated with regional decreased count density in

the inferior myocardial wall of the left ventricle (Miles et al., 1999). This artefact is illustrated in *figure 2.1*.

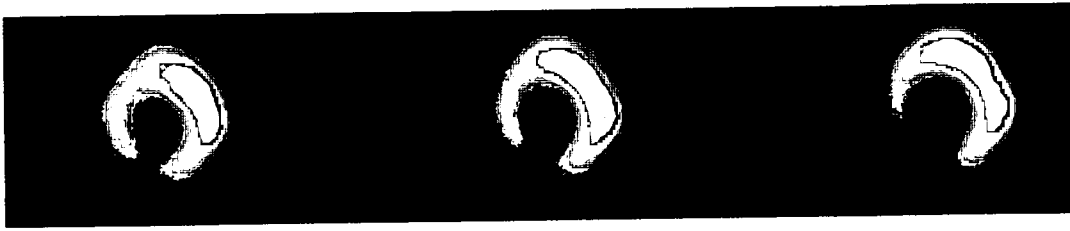


Figure 2.1: *Short axis slices illustrating the effect of diaphragm attenuation in the inferior region of the left ventricle.*

Photons undergo severe attenuation in men with raised diaphragms and women with larger breasts (Tsui et al., 1994b; DePeuy and Garcia, 1989). The magnitude and extent of both diaphragm and breast tissue artefacts may vary from patient to patient and depend on the size, density, shape and location of the diaphragm and breast relative to the myocardium. The best way to avoid the limitation of specificity is to detect and eliminate artefacts (DePeuy and Garcia, 1989; DePeuy 1994).

SPECT imaging is not only degraded by attenuation artefacts, but it is also affected by Compton scatter and the detector response function (Tsui et al., 1994a). Inclusion of scatter in the image degrades the reconstructed image by blurring fine detail and lowering contrast. This may lead to an inaccurate determination of the dimensions of specific regions of interest (ROIs). In cardiac studies, scatter artefacts of the left ventricle are due to a complicated contribution of activity in adjacent organs. For example, the scatter originating from the right ventricle contributes to the septal wall of the left ventricle and the scatter from the liver contributes to the inferior wall (Tsui et al., 1998).

An important characteristic of the collimator system of a scintillation camera is the spatial resolution that is characterised by the detector response function (Beck et al., 1973). Loss of resolution produces blurred images and causes difficulties in the determination of physical dimensions like volume and area. The detector response function varies with distance of the patient's organ from the camera. During the rotation of the camera, the distance of the patient's organ from the camera varies and so does the detector response function. The distance-dependent detector response can result in wall thickness artefacts that may imitate a myocardial defect (Maniawski et al., 1991).

An artefact in SPECT images may be determined by combined factors i.e. photon attenuation, photon scatter and degradation in resolution with distance from the collimator. The effects of these three factors have already been mentioned and their complexity in myocardial SPECT is illustrated in *figure 2.2* (Galt et al., 1999). In *figure 2.2* the detector in the top position represents the acquisition at the anterior region of the heart, while the second detector represents the acquisition in the lateral view. *Figure 2.2A* illustrates that the detector in the anterior view may collect a photon being emitted from the myocardium after traversing a small amount of tissue. The photons collected by the detector in the lateral view travel through a larger amount of tissue with more complicated attenuation effects since lung, bone and muscle tissue are included in the path.

The photons may undergo Compton scatter and may be detected as if they originated from the other position and this may be complicated by tissue on the path to the detector

(figure 2.2B). The spatial resolution varies around the patient as the distance between the point in the patient and camera changes (figure 2.2C).

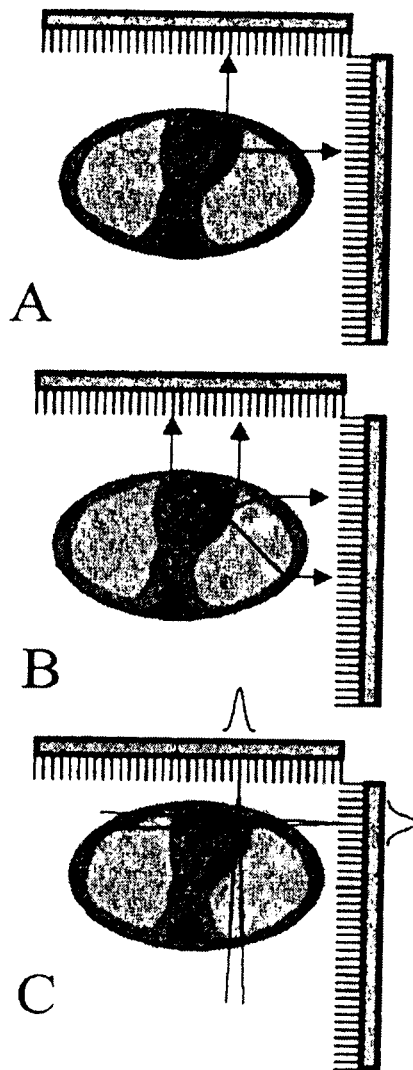


Figure 2.2: Physical factors that complicate the myocardial perfusion imaging include: (A) non-uniform attenuation, (B) Compton scatter and (C) distance dependent resolution.

Photon attenuation refers to the loss of photons due to the interaction with tissue causing absorption and scattering of photons (Curry et al., 1990). It depends on the photon

energy, the density of the medium through which the photon travels and the distance that the photon travels.

Let I_0 be the number of photons before interacting with the medium of thickness x . The number of the transmitted photons (I), is given by *equation 2.1*

$$I = I_0 e^{-\mu x} \quad 2.1$$

The attenuation coefficient of the medium, μ , depends on the photon energy and the density of the attenuating medium (Tsui et al., 1994a). *Equation 2.1* assumes narrow-beam geometry, and broad beam geometry is not strictly described by this equation. The use of broad-beam geometry in a uniform medium results in a smaller attenuation coefficient compared to narrow-beam geometry due to the presence of scatter. For example, the broad and narrow beam μ values for Tc-99m in soft tissue are 0.012mm^{-1} and 0.015mm^{-1} respectively. The term $e^{-\mu x}$ represents the fraction of photons that are not attenuated over a distance x and includes the effects of photons lost to Compton scatter and absorption.

In SPECT, attenuation of photons imposes important limitations on the quantification of activity within a specific region of the body (Almquist et al., 1990). In the clinical situation more attenuation will be encountered in obese than in thin patients. Attenuation of the photons will also be strongly dependent on the location of the source. Anatomical structures and non-uniform attenuation properties in the chest complicate the attenuation

effect. The thorax area consists of muscle, lungs and bone tissue all with different attenuation properties (Tsui et al., 1998).

The scatter of a photon results when the incident photon transfers part of its energy to a recoil electron and deflects the photon from its initial direction of travel. Scatter events in the image are caused by photons that are emitted in one direction but scattered in the object into a direction detectable by the SPECT camera. These scattered photons carry misleading information and they limit image contrast and lesion detection (Ljungberg et al., 1994). When a photon with energy of 140keV is scattered through an angle of 30° it will lose 3.5% of its energy that corresponds to about 5keV. This results in a photon being detected well within the 15% (21keV) energy window used in clinical studies. Photon scatter has a higher probability in broad beam geometry than narrow beam geometry. It also increases with the thickness and composition of the medium. In myocardial studies photon scatter is complicated by the inhomogeneity of the thorax. After scattering, photons emitted from the liver for instance, appear to originate from the inferior myocardial wall and thus lead to reduced image contrast and reduced lesion detection in myocardial SPECT imaging.

Spatial resolution refers to the ability of the detector to provide sharpness and detail in an image (Sorenson and Phelps, 1987). The collimator is the limiting factor in the spatial resolution of the system. A collimator with smaller holes may improve spatial resolution but the detection efficiency will be reduced. Spatial resolution deteriorates with an increase in distance between the source and the detector. This deterioration in resolution

is given by the detector response function. As the camera rotates around the patient, the centre of rotation (COR) is the only point in the patient that maintains the same distance from the camera head, and the spatial resolution at the COR is radially symmetric and isotropic (Tsui et al., 1998). The spatial resolution at any other point is anisotropic (Tsui et al., 1998). Such spatially varying resolution can lead to significant distortion in the reconstructed images especially for 180° acquisitions (Knešaurek et al., 1989).

2.2 Attenuation compensation

2.2.1 Introduction

Attenuation of photons in the surrounding medium has already been mentioned in the previous paragraph. Attenuation degrades the specificity of cardiac SPECT imaging because coronary artery disease (CAD) can be falsely reported due to inferior attenuation artefacts. The attenuation coefficient of the attenuating medium gives the probability that a photon will be attenuated by that medium. In order to compensate for attenuation through a medium, the attenuation coefficients of the medium need to be known accurately.

2.2.2 Conventional methods

The problem of attenuation in SPECT has proven to be difficult to solve and several correction methods have been suggested (Tanaka, 1983; Chang, 1978; Walters et al., 1981). The methods proposed by Sorenson (1984) and Chang (1978), namely pre-reconstruction and post-reconstruction methods respectively are commonly used in commercial systems. These methods assume a uniform attenuating medium and are used effectively in applications where attenuation is approximately uniform such as liver and

abdomen studies. Both methods require that the outside body contours be defined. In practice, methods commercially available often fit the body with an ellipse defined either by an edge detection operator or a count threshold of the emission data.

Sorenson's method is based on attenuation correction before the processing of data (pre-processing); it modifies the projection data by an average attenuation factor (Sorenson, 1984). This method is based on the conjugate counting technique adapted from planar nuclear medicine techniques for quantitative *in vivo* measurement of radioactive distributions (Sorenson, 1984). Examples of these counting techniques are the geometric mean (GM) and arithmetic mean (AM) methods. The GM of conjugate views strongly depends on body thickness while it is weakly dependent on source thickness (Tsui et al., 1994a). On the other hand the AM method strongly depends on body thickness and weakly depends on both source depth and source thickness (Tsui et al., 1994a). The GM and AM compensation methods are easy to implement and show good results for a single point source in a uniform medium. These compensation methods are limited in the situation of multiple sources and when the source depth and thickness are not known. Isolated sources tend to be combined in the reconstructed image when the GM method is used, and the reconstructed image using the AM method shows a decrease in counts in the centre, thus showing its source dependency (Tsui et al., 1994a).

Chang's method is based on attenuation correction after data processing (Chang, 1978). It is probably the most widely used method for attenuation correction. A correction factor $C(x,y)$ is calculated at each image point as an average attenuation factor over all

projection angles. In order to correct for homogenous attenuation, the average attenuation coefficient and the body contours are required (Tsui et al., 1994a). When dealing with non-uniform attenuation, the correction factor can be calculated from a known attenuation coefficient distribution. The corrected image is obtained by multiplying the reconstructed image with the correction factor. Compensation using the Chang method tends to over- and under correct some parts of the image (Tsui et al., 1994a).

These conventional methods may be useful in areas with a uniform attenuating medium. The inhomogeneous thorax region consists of tissue with different attenuation properties. Therefore these methods should not be applied to myocardial perfusion SPECT studies.

2.2.3 Transmission-based attenuation correction

Accurate attenuation correction in the thorax region requires that the patient's specific attenuation coefficients be known accurately. Attenuation corrections for inhomogeneous medium are based on the use of attenuation coefficients obtained from transmission studies using X-ray computed tomography (CT) or radionuclide sources. The use of X-ray CT to obtain transmission images has the advantage of producing a good spatial resolution and a statistically accurate image. However the use of X-ray CT will require translation, rotation and scaling to match the SPECT image (Koral et al., 1988). The different photon energy used for SPECT as compared to X-ray CT, i.e. 140keV (^{99m}Tc) and 120kVp (mean energy 40keV) respectively, affects the value of the attenuation coefficient. Translation from the Hounsfield value to an attenuation coefficient is not straightforward and then it has to be energy-translated to a value corresponding to the 140 keV emission energy. Furthermore the CT and SPECT images have to be registered

since two different imaging modalities are used. Therefore transmission images based on X-ray CT imaging are not recommended.

Transmission imaging using a radionuclide has been reported as the preferred technique to obtain attenuation information in order to compensate for the attenuation of photons in the patient (Bailey et al., 1987; Tsui et al., 1989; Frey et al., 1992; Jaszczak et al., 1993; Ficaro et al., 1994). Bailey et al (1987) proposed a method to simultaneously acquire emission and transmission tomography data in order to produce emission information and a map of attenuation coefficients for the body. The method was based on using a single detector and a radionuclide flood source attached to a rotating gamma camera with parallel hole collimation. This method used simultaneous acquisition rather than sequential acquisition since the latter results in problems associated with repositioning of the patient in order to align the emission and transmission data. The proposed method used different radionuclides for transmission and emission studies. The radionuclides were separated by pulse height energy discrimination.

Transmission images are converted to attenuation projections using *equation 2.2*:

$$\mu_{\theta}(i, j) = \ln \left[\frac{N_0(i, j)}{N_{\theta}(i, j)} \right] K \quad 2.2$$

Where $\mu_{\theta}(i, j)$ is the line integral of the attenuation coefficients of the object at projection θ for pixel (i, j) , $N_0(i, j)$ is the reference projection, $N_{\theta}(i, j)$ is the θ^{th} transmission projection and K is a scaling constant. $N_0(i, j)$ is obtained from a transmission study

without any attenuating medium between the detector and the source. $N_{\theta}(i,j)$ are the transmission images obtained from the patient. *Equation 2.2* results in the normalisation of the reference projections with respect to the transmission projections. Non-uniformities in the projections will therefore be corrected for. Non-uniformities can occur due to the transmission source not being uniform or detector non-uniformities. The attenuation projections are then reconstructed using a suitable reconstruction algorithm.

The reconstructed attenuation projections are used to compensate for attenuation of emission photons at specific points. The method of Bailey et al. (1987) has the ability to accurately display the patient's contour, display the subject anatomy and accurately determine the value of μ for each voxel within the field of view (FOV). Bailey's method uses an uncollimated flood source thus producing a large amount of scatter. Tsui et al. (1989) considered the collimation of the flood source to reduce scatter. This caused a reduction in the radiation dose to the patient and staff and improved the image resolution.

There are different designs available for transmission imaging with SPECT systems (*figure 2.3*). The first commercial system to integrate the transmission-computed tomography (TCT) is a triple detector system that positions a lightweight, low dose line source at the focal point of one of the symmetric fan beam collimated detectors, (*figure 2.3A*). Such a design is based on the work of Tung et al. (1992). This system used fan beam collimation for both emission and transmission imaging. The external radiation source is placed at the focal point of one of the collimators. Detector 1 acquires data from transmission and emission sources at different energies while detectors 2 and 3 acquire emission data only. This system enables simultaneous acquisition of transmission and

emission without an increase in patient scanning time and with high counting efficiency (Galt et al., 1999). The disadvantage of the system is the truncation of the body portion in the transmission data by the fan beam geometry collimation. Without any compensation the truncated image will contain image artefacts. The use of the maximum likelihood (ML) iterative reconstruction algorithm with expectation maximisation (EM) by Lange and Carson (1984) can minimise the truncation (Gregoriou et al., 1998). The use of an asymmetric fan beam collimator (King et al., 1995; Chang et al: 1995) or a parallel slant hole collimator (King et al., 1996) will also reduce truncation artefacts.

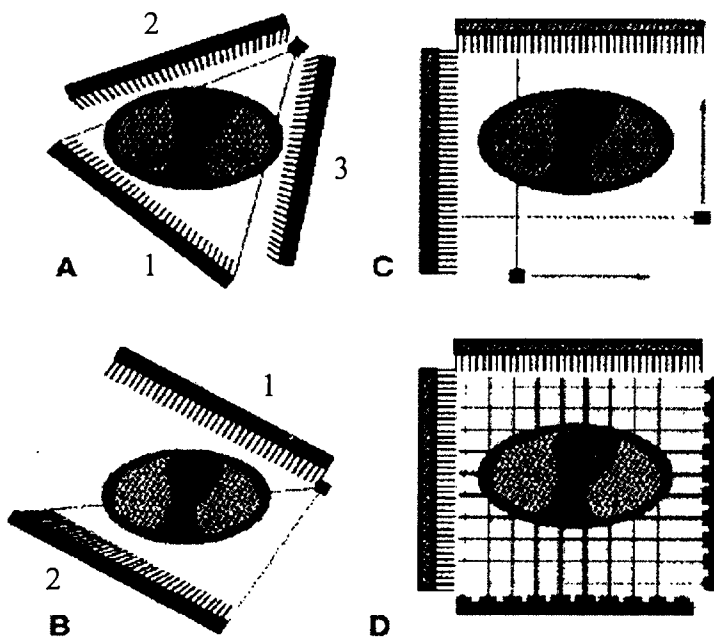


Figure 2.3: *An illustration of different transmission computed tomography systems.*

Another approach used for transmission imaging is the use of opposing detectors as proposed by Hawman et al. (1994) and Chang et al. (1995) and shown in *figure 2.3B*. The

line source is placed next to the emission detector (1), opposite the second detector. Detector 2 is mounted with an asymmetric fan beam collimator focused on the line source. The line source is shielded to the emission detector (1) and detector 1 only acquires data from the emission source. Detector 2 acquires both emission and transmission data for a 360° rotation. In this approach only half of the emission field of view is sampled by the transmission scan at a given planar projection and thus increases the patient scanning time (Galt et al., 1999).

Most manufacturers using a 90° dual detector SPECT system have developed attenuation compensation hardware based on the scanning line source. This was first described by Tan et al. (1993) and is illustrated in *figure 2.3C*. This approach uses conventional parallel hole collimation and 1 or 2 collimated line source(s) scanning across the field of view of the camera. Transmission and emission data acquisition can be performed simultaneously or separately (Galt et al., 1999). This system is mechanically more complex than a fixed line source system and has a reduced sensitivity compared with the diverging geometry since the source is positioned over a given region of the patient for a short portion of the scan time (Miles et al., 1999). The use of parallel hole collimation lowers the geometric efficiency and therefore a source with an increased strength is required. Such high source strengths result in higher scatter-to-primary photon ratios and higher patient doses than occur with a line source placed at the focal line of a fan beam collimator (Gullberg, 1998). Scanning line source systems are available that use an electronic window that moves simultaneously and opposite the external source to separate transmission and emission data (Tan et al., 1993; Miles et al., 1999). Beekman et

al. (1998) has replaced the scanning line source with a scanning point source and used parallel hole collimation with half-fan beam collimation. The point source is scanned along the focal line of a half fan beam collimator for the application in simultaneous transmission and emission SPECT. The improvement reveals a reduction in the scatter-to-primary count ratio and it requires a low-activity point source. This design is economically beneficial and reduces radiation exposure to the patients and staff. Half-fan beam TCT has a higher resolution compared to parallel hole TCT and it eliminates truncation caused by the fixed symmetry fan beam system (Beekman et al., 1998).

The fourth approach uses an array of line sources positioned close enough to each other in order to appear as a continuous distribution to the scintillation detector (*figure 2.3D*). The central sources have the highest source strength to compensate for greater attenuation in the centre and the source strength gradually decreases to the sides. This approach maximises the counts received through the more attenuating central regions of the patient and minimises the flux at the directly exposed regions of the detector that could result in the contribution of the high count rates. These count rates can impair the detector performance causing dead time errors and errors in the accuracy of the attenuation coefficient values.

Corbet and Ficaro (1999) reported some of the requirements that are necessary for an ideal SPECT TCT system. The system should be simple to use and maintain. A TCT system should result in minimal additional exposure to the patients and staff and it is important that they have a reasonable operating cost, for example such as the source

replacement cost should be taken into account. Almeida et al. (1998) studied the absorbed dose resulting from transmission scanning for both SPECT and PET (positron emission tomography) imaging using ^{153}Gd and ^{68}Ge simultaneously. The study performed with phantoms reveals that the effective dose of radiation absorbed in a patient during transmission scanning is negligible to those obtained from radionuclide injection in routine nuclear medicine procedures. The effective dose (ED) values derived from the cardiac studies were $1.9 \times 10^{-6} \pm 0.4 \times 10^{-6} \text{mSv/ MBq.h}$ and $7.7 \times 10^{-4} \pm 0.4 \times 10^{-4} \text{mSv/ MBq.h}$ for SPECT and PET transmission measurements respectively. ED values derived from the brain studies were $5.2 \times 10^{-7} \pm 0.4 \times 10^{-7} \text{mSv/ MBq.h}$ and $2.7 \times 10^{-4} \pm 0.2 \times 10^{-4} \text{mSv/ MBq.h}$ for SPECT and PET transmission measurements respectively. Radiation dose, therefore, does not present a limit to the generalised use of transmission measurements in clinical SPECT and PET.

2.2.3.1 Selection of a radionuclide source for transmission imaging

Transmission imaging provides useful information to calculate attenuation coefficient maps, therefore the choice of the TCT source has to be considered carefully. TCT requires a transmission source that is relatively inexpensive and commercially available. It is required that the source has a long half-life for clinical use to avoid frequent replacement. The transmission and emission data should be separable with NaI (TI) gamma spectroscopy (Bailey et al., 1987). $^{99\text{m}}\text{Tc}$ is commonly used as an emission source in the myocardial perfusion studies. The properties for transmission sources usually used with $^{99\text{m}}\text{Tc}$ are given in *table 2. 1* and will be discussed briefly.

Table 2.1: *Some proposed transmission sources used with ^{99m}Tc as emission source.*

Radionuclide	Half life	Energy	Proposed by
^{153}Gd	240days	97.4keV 103.2keV	Bailey <i>et al.</i> , 1987
^{99m}Tc	6.02hrs	140.5keV	Frey <i>et al.</i> , 1992 Welch <i>et al.</i> , 1994
^{123m}Te	119.7days	159keV	Wang <i>et al.</i> , 1995
^{139}Ce	137.5days	166keV	Naudé <i>et al.</i> , 1997

Gadolinium-153 (^{153}Gd), proposed by Bailey *et al.* (1987), has emerged as a popular choice for transmission imaging largely because of its long half-life. It has dual photopeaks with an average energy of 100keV but it may be limited by high k-shell X-ray production with energy of 40 and 50keV that contributes to the patient dose. The additional X-rays increase the detector's count rate without contributing to transmission image formation. Such X-rays can however be eliminated by copper filtration.

^{99m}Tc may also be used as a transmission source because of its availability. The use of ^{99m}Tc has the advantage that there is no need for attenuation coefficient conversion when using ^{99m}Tc also as emission source. However the short half-life of ^{99m}Tc of 6.02hours will require the line source to be filled daily and the absence of an energy difference between transmission and emission sources can result in problems of enormous cross-contamination of transmission and emission information.

Wang *et al.* (1995) reported a metastable transmission source ^{123m}Te with primary photon energy 159keV and half-life of 119.7days. The small energy difference between ^{123m}Te

and ^{99m}Tc (emission source) has the advantage of an accurate calculation of attenuation coefficients but the simultaneous acquisition with both sources results in difficulty to resolve them with the present scintillation cameras due to their energy resolution of 9%.

Naudé et al. (1997) proposed the use of ^{139}Ce as a transmission source. It is a mono-energetic source with energy of 166keV and half-life of 137.5days. The larger energy difference between ^{139}Ce and ^{99m}Tc resulted in a better separation of transmission and emission data, when acquired simultaneously (Du Raan et al, 2000).

In order to avoid crossover between the transmission and emission energy windows during simultaneous data acquisition, the energy difference between two sources must be large enough. The spectral crossover characteristic depends on the particular selection of emission and transmission sources. When the choice of the emission source is ^{99m}Tc with photon energy of 140keV it can be scattered and detected in the ^{153}Gd energy window at 100keV. When ^{201}Tl with photon energies of 72keV and 167keV is used as an emission source with the ^{153}Gd transmission source, transmission data can be scattered and detected in the ^{201}Tl energy window of 72keV (Galt et al., 1999). Naudé (1998) claimed that the use of a transmission source of higher energy than the emission source was preferred to avoid the problem of cross contamination from the emission window into the transmission image to be much bigger.

2.2.3.2 Simultaneous or sequential data acquisition

SPECT imaging studies may be performed using sequential and simultaneous modes for emission and transmission data acquisition. Sequential mode allows emission and transmission data to be acquired separately, this mode therefore avoids cross talk between

the emission and transmission data. The simultaneous mode, result in contaminated data, however the availability of dual and triple detector scintillation cameras makes it possible to acquire emission and transmission data simultaneously (Naudé, 1998).

Matsunari et al. (1998) observed in both phantom and clinical studies that misalignment between emission and transmission scans can introduce serious errors after the SPECT data have been corrected for attenuation. Misalignment is associated with patient motion and can be present in the sequential mode. For example in cardiac phantom studies a 7mm (1pixel) shift produced up to 15% change in relative regional activity (Matsunari et al., 1998).

Ogasawara et al. (1998) observed that the quantitative values obtained with sequential and simultaneous acquisition modes were similar in phantom studies. However the advantage with the simultaneous mode is that it allows a shorter examination time thereby reducing the burden for patients and it can avoid misalignment between emission and transmission data. Therefore the simultaneous mode was preferred for this study (Ogasawara et al., 1998).

2.2.4 Emission based attenuation correction

A disadvantage of transmission based attenuation correction imaging is that additional hardware is necessary to mount the external transmission source, and thus increase the cost of the system. The external source may be expensive and the higher strength of activity adds to the radiation dose to the patient and staff.

Emission based attenuation correction was used by Madsen et al. (1997) to correct for attenuation in the thorax during myocardial imaging. This approach was based on the assumption that for practical purposes the thorax consists of two types of tissue i.e. the lung and soft tissue, and these tissues are almost uniform within themselves. If the assumption is true, then the only information necessary for the creation of an attenuation map is the definition of boundaries of the lungs and the patient's body contour. Tsui et al. (1998) reported that the average attenuation coefficient of lung tissue was about one third that of soft tissue. Therefore, there is a large difference in the attenuation effect between them. In the article by Madsen et al. (1997), the body contour was defined first through a radial search for the local maxima at 32 angles around the image of the body outline resulting from a flexible radioactive body binder containing ^{99m}Tc . These points were fitted with a Fourier series to eliminate any bad points, and the connected outline of the body was formed. This process was repeated on subsequent slices. The interior of the contour was filled with a value corresponding to the attenuation coefficient for unit density soft tissue. The boundaries of the lungs were determined by applying a count threshold to the ^{99m}Tc -labelled macro aggregated albumen (MAA) images that were obtained from the patient. All pixels within the lung that were greater than 20% of maximum lung count value were set to the mean attenuation coefficient for lung tissue from the PET transmission measured value. Since the study was done with SPECT, scaling from PET was necessary for the appropriate photon energy. Attenuation maps were generated by assigning appropriate attenuation coefficients for the gamma rays used in the SPECT study to the areas defined by the boundaries. Mean attenuation coefficients were in good agreement with the mean attenuation for the tissue reported in the literature

(ICRU, 1989), and they were consistent with the assumption that tissue attenuation coefficients did not vary widely among individuals.

These fixed maps were used for attenuation correction of the emission data acquired by ^{99m}Tc -MIBI in stress and ^{201}Tl at rest. Phantom results have shown that attenuation artefacts were eliminated and the variation in the mean count density was less than 10% across the entire heart after the use of emission based attenuation correction (Madsen et al., 1997). Emission-based attenuation correction removes the attenuation artefacts in the inferior wall thereby improving the diagnosis of CAD. The emission-based systems were considered to be inexpensive because they did not need extra hardware. No extra cost is required as for the transmission system and transmission source replacement. These systems gives a reduced radiation dose to the patients and staff compared to transmission-based methods and they are not limited to any SPECT system. They have an advantage of obtaining emission data without the contamination of transmission data.

Such attenuation correction techniques may be excluded for patients with pulmonary disease when defining the lungs using ^{99m}Tc -labelled macro aggregated albumin (MAA). This attenuation correction technique requires more processing time over that required for routine SPECT studies because multiple reconstructions are needed. Another disadvantage for the use of such an approach is the need for two separate SPECT acquisition studies, with the resultant potential for misregistration. Therefore this attenuation technique needs further improvement before it can be routinely applied for clinical studies.

2.3 Scatter correction

Photon scatter can result in the misplacement of counts. The presence of scatter in the image limits the accuracy of the quantification of activity and reduces the image contrast by including low frequency blur in the image. Scattered photons can originate from the surrounding attenuation medium, imaging table or scintillation camera (Zaidi, 1996). In left ventricular myocardial perfusion studies the scattered photons can also be due to the photons from the liver and right ventricle, therefore scatter compensation is necessary to improve the quality of SPECT imaging.

Scatter compensation methods for SPECT require estimation of the number of scattered photons in each pixel of the image. This is complex because the scatter component of the image depends on the energy of the photon, the energy window used, the composition and the location of the source, and the scattering medium (Frey and Tsui, 1994). Ideally scatter can be separated from primary photons because of the difference in energy, but the poor resolution of the NaI (Tl) crystal used in a gamma camera system makes it difficult to discriminate all scattered photons from primary photons (Sorenson and Phelps, 1987).

One attempt to reduce scatter was suggested by Harris et al (1984) using an attenuation coefficient less than that used for narrow beam geometry. For example, 0.012mm^{-1} for $^{99\text{m}}\text{Tc}$ was used instead of 0.015mm^{-1} . However, the effect of scatter is object-dependent, this correction method did not take this into account and therefore resulted in large quantification errors. Therefore this method was not recommended for this study.

Methods of scatter correction can be divided into three broad categories: energy window-based methods, deconvolution-based methods and reconstruction-based methods.

Energy window based methods estimate the amount of scatter in the image and explicitly correct for it. A widely used energy based method is the dual window subtraction method suggested by Jaczszak et al. (1984) for ^{99m}Tc . It was based on the acquisition of a scatter photon image in a secondary window that was placed below the photopeak window in the Compton region. The acquired scatter from this secondary window was assumed to be qualitatively equal to the scatter in the photopeak window with respect to the spatial distribution, to differ quantitatively by a factor of k . k was determined by the ratio between the scatter in the photopeak window and the counts in the secondary energy window. An accepted value for k is 0.5 (Ljungberg et al., 1994). A drawback of this method was the determination of the scatter multiplier k , which depends on the specific patient and imaging situation (Koral et al., 1990).

Ogawa et al. (1990) proposed the triple energy window (TEW) method. It uses three energy windows i.e. a photopeak energy window with two narrow sub-windows on either side of the photopeak energy window. The correction in this method was performed for each pixel in the projection data based on the positional dependency of photon scattering (Hashimoto et al., 1999). The scatter component in the main window is estimated from the linear fit of the data from the adjoining two smaller energy windows. The TEW algorithm is easy to implement in routine clinical examinations, as it does not require any system-specific calibration (Ljungberg et al., 1994).

King et al. (1992) proposed a dual peak window (DPW) method where a single 20% energy window was divided into two energy windows. The method was based on the assumption that there was an empirical relationship between the ratio of the counts collected in the two energy windows and the scatter fraction. The method has been shown to provide a good estimation of the scatter response function (Tsui et al., 1994a). Ljungberg et al. (1994) has shown that the method is difficult to implement for the extended sources distribution due to its sensitivity to noise compared to the TEW and dual window subtraction methods. Another approach called the channel ratio (CR) technique showed promising results for planar images (Pretorius et al., 1993; Naudé et al., 1996) and was also based on two energy windows spanning the photopeak of the energy spectrum. The CR depends on the stability of the energy window setting and requires a pre-calibration. Energy based methods could provide only approximate scatter compensation and may result in an increase in image noise (Buvat et al., 1995).

Other methods are the deconvolution-based methods and they are based on data from a single window (Axelsson et al., 1984). These techniques assume that the scattered photons within the image can be modelled by a function independent of the medium distribution. The scatter component was removed or convoluted from the image by restoring filtering methods (Floyd et al., 1985; King et al., 1991). Although they can provide approximate scatter compensation, they are limited by their spatial invariant response function such that they result in inaccurate scatter compensation.

Reconstruction based scatter correction (RBSC) methods incorporate compensation for Compton scatter directly into iterative reconstruction (Beekman et al., 1993). The compensation in this method was achieved, in effect, by mapping scattered photons back to their point of origin (Kadrmas et al, 1998). This method can be used to reconstruct data obtained from an energy window that accepts primarily scattered events. Compensation using this method leads to lower noise levels compared to subtraction based methods i.e. window and deconvolution based methods (Kadrmas et al, 1998). The modelling of scatter for radionuclides with more than one emission energy, for example ^{201}Tl is more difficult than for single emission energy radionuclides such as $^{99\text{m}}\text{Tc}$. The modelling of scatter for a non-uniform attenuator like the thorax is even more difficult. Although the RBSC methods accounted for the increased amount of scatter from the sources in the scattering medium, their main disadvantage was that they are computationally intensive, which resulted in longer reconstruction times (Kadrmas et al., 1998). The RBSC technique is therefore considered to be clinically limited.

2.3.1 The triple energy window scatter correction technique.

The triple energy window technique (TEW) was the scatter correction method used in this study and incorporates position-dependent Compton scattering of photons as proposed by Ogawa *et al.* (1991). As mentioned previously, the TEW technique employs three energy windows for data acquisition. The main window was centred at the photo-peak and two narrow sub-windows were positioned on the adjacent sides of the main energy window (*figure 2.4*). The scatter fraction in the main window was estimated by a trapezoidal approximation based on the counts in the subwindows and was removed by subtraction (Ogawa et al., 1991; Ishihara et al, 1993)

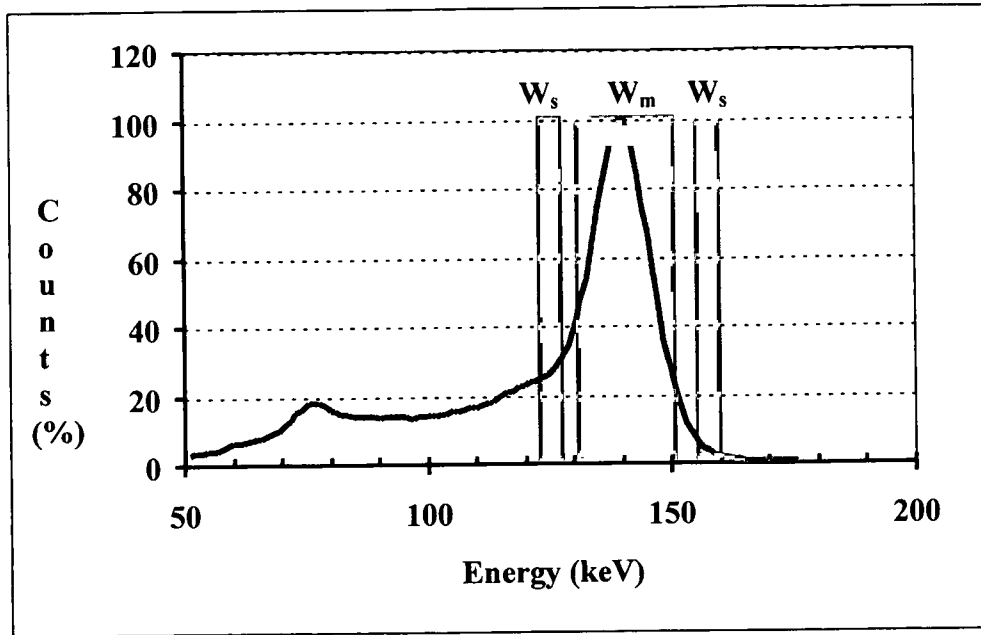


Figure 2.4: Energy window selection for TEW scatter correction technique.

For the main window the total counts (C_{total}), was assumed to be composed of primary photons counts (C_{prim}) and those due to scattered photons (C_{scat}). Thus the counts obtained from the primary photons were given by:

$$C_{prim} = C_{total} - C_{scat} \quad 2.3$$

The C_{scat} was estimated from the count data C_{left} and C_{right} acquired within the two respective sub-windows, where each sub-window has a width of W_s . The width of the main window was W_m . The counts obtained from the scattered photons could be estimated from the trapezoidal region having an average left height of C_{left}/W_s , an average right height of C_{right}/W_s and a base of W_m . The total scattered counts was therefore given by:

$$C_{scat} \cong \left(\frac{C_{left}}{W_s} + \frac{C_{right}}{W_s} \right) \times \frac{W_m}{2} \quad 2.4$$

Thus the primary counts were estimated as

$$C_{prim} = C_{total} - \left(\frac{C_{left}}{W_s} + \frac{C_{right}}{W_s} \right) \times \frac{W_m}{2} \quad 2.5$$

When mono-energetic photons are emitted, the counts, C_{right} , in the high-energy sub-window will be less than 5% of those in the main window and could usually be omitted (Ogawa et al., 1991). The left sub-window could be enlarged to improve the signal-to-noise ratio (Hashimoto et al., 1997). Based on Monte Carlo simulations it has been shown that the use of only a main window and lower sub-window for image acquisition was sufficient for ^{99m}Tc (Ogawa et al., 1990; Ogawa et al., 1991). Therefore, depending on the nuclide used, data were acquired in two or three energy windows.

Different energy window widths used for data acquisition have been proposed by various authors (Ishihara et al., 1993; Ljungberg et al., 1994). The use of a narrower analyser window for scatter rejection reduced the recorded counting rate and increased the statistical noise, a trade-off between statistical noise and scattered photons resulted (Sorenson and Phelps, 1987). Ljungberg et al. (1994) concluded that the TEW technique was easy to implement, as no system-specific calibration was required. Naudé (1998) results from phantom studies using ^{99m}Tc as the emission source and the TEW scatter correction approach, concluded that this approach reduced the amount of scatter data contributing to the quantified values and the accuracy of the final quantification was improved.

2.4 Compensation of detector response function

The collimator detector response (CDR) of a typical scintillation camera system used in SPECT is spatially variant i.e. the spatial resolution degrades as the distance from the collimator increases. Restoring filters like Metz (Metz, 1969) and Wiener (King et al., 1983) provided an efficient method to correct for the collimator detector response (King et al., 1991). In these methods an average or effective collimator response function was used. These filters were based on the principle that the point source response function (PSRF) may be regarded as a stationary blurring function (Tsui et al., 1994b). Since the CDR varies with distance, these methods do not provide exact solutions.

Analytic methods to solve the SPECT reconstruction problem with distance varying CDR have been proposed. Earlier approaches required either information that is impossible to obtain in practice (Zeeberg et al., 1987), for example assuming collimator parameters that are not fully met in practical collimators (Pan et al., 1997), or made unrealistic assumptions about the shape of the detector response function (Appledorn, 1989).

Another approach was to use the frequency distance principle (FDP) which stated that points at a specific source-to-detector distance correspond to specific regions in frequency space of the sinogram's Fourier transform (Galt et al., 1999). This technique allowed separation of the projection data in sinogram frequency space as a function of distance from the collimator (Tsui et al., 1998). Resolution recovery was obtained by applying the spatially variant inverse filter to the sinograms. Although such sinograms

were relatively fast, they gave approximate compensation and care must be taken to prevent amplification of high frequency noise (Tsui et al., 1998).

Resolution recovery could also be included in iterative reconstruction methods (Liang, 1993). The use of such methods results in superior image quality and quantification that is more accurate compared to the image restoration filtering technique. It was found that fully three dimensional (3D) reconstruction provides both improved spatial resolution recovery and lower noise level compared with two dimensional (2D) reconstruction (Tsui et al., 1994b). However, the 3D-image compensation approach requires more computational time. A prerequisite for the iterative technique was that the 3D PSRF must be known. However it was involve the handling of a large amount of data.

Iterative methods yield most effective compensations for CDR, although they are computation intensive. However, Naudé (1998) observed that the detector response correction did not have a substantial effect on quantification in phantom.

2.5 Single Photon Emission Computed Tomography reconstruction algorithms

2.5.1 Introduction

Planar imaging is routinely used to image the object to produce 2D projections of a 3D-object distribution. However the image quality is seriously affected by the superimposition of non-target activity, which restricts the measurement of the patient's organ function and prohibits accurate quantification of that function. The implementation

of SPECT overcomes such superposition of activity (Larsson, 1980). SPECT provides tomographic images that are 2D representations of structures lying within a selected plane or depth in a 3D object. In tomographic images, the detector is moved around the object to acquire photon data at discrete angles typically over 180° or 360° .

The use of SPECT improves contrast, spatial resolution, spatial localisation, detection of abnormal function and leads to great improvement in quantification (Webb, 1988). Many physical factors may affect quantitative accuracy, so it is important to implement a reconstruction algorithm that will improve the above-mentioned factors.

Chornoboy et al. (1990) mentioned the physical factors that an accurate reconstruction algorithm has to incorporate in SPECT imaging. The reconstruction algorithm must consider the radioactive decay process as a random process resulting in poor data statistics. The reconstruction algorithm must take into account the depth-dependent response function caused by scattering and the collimation geometry of the detector. The reconstruction algorithm should also address the influence of photon absorption and scatter.

Analytic and iterative algorithms have emerged as the main reconstruction algorithms. A short description of the analytic methods will be presented but the emphasis will be more on the iterative methods because of their accuracy in comparison to analytic methods.

2.5.2 Analytical reconstruction algorithms

The common characteristics of analytic methods are that they utilise exact formulae for the reconstruction image density. The most popular examples of these methods are the back-projection (BP) and filtered back-projection (FBP) algorithms (Brooks and Di Chiro, 1976). FBP is routinely used in Nuclear Medicine departments.

2.5.2.1 The Back-projection reconstruction algorithms

The first attempts at reconstructing tomographic images used the back-projection (BP) reconstruction algorithm of Brooks and Di Chiro, 1976. In this technique the data from the corresponding rows of pixels in the original image were projected onto a reconstruction matrix from the same angle at which each image was originally acquired and were added together (Hendee, 1984). It was assumed that the absorption along a ray path was due to a uniform distribution of density along the path length. The process of this reconstruction was given by:

$$\hat{f}(x, y) = \sum_{j=i}^m p(x \cos \phi_j + y \sin \phi_j, \phi_j) \Delta\phi \quad 2.6$$

Where ϕ_j is the j^{th} projection angle, $\Delta\phi$ is the angular distance between the ray projections p and the summation extended over all m projections. The symbol \hat{f} indicates that the predicted radionuclide distribution was not equivalent to the true distribution $f(x, y)$. The BP provided a blurred image, representative of the object however it contained spoke or star artefacts (Webb, 1988).

2.5.2.2 Filtered Back-projection reconstruction algorithms

The most commonly used reconstruction algorithms in SPECT are based on filtered back projections (Tsui et al., 1994a). This algorithm aimed at providing a blur-corrected image. The projection data are convolved with a ramp filter to eliminate the blurring effect before the data are back-projected. This algorithm provides both speed and accuracy for image reconstruction (Hendee, 1984). The filter used has negative lobes on either side of the positive core so that in summing the filtered back-projection, positive and negative contributions cancel outside the core. The process of this reconstruction may be expressed mathematically as:

$$p^*(r, \phi) = \int_{-\infty}^{\infty} |k| P(k, \phi) e^{2\pi i k r} dk \quad 2.7$$

where $p(r, \phi)$ represents the ray projection with ϕ indicating the angle of the ray and r the distance from the origin respectively; $p^*(r, \phi)$ the filtered ray projection; $P(k, \phi)$ the Fourier transform of $p(r, \phi)$ with respect to r and k the filter factor. The function $p(r, \phi)$ is manipulated before being back-projected by filtering.

The ramp filter has the disadvantage of enhancing the noise because of the high frequency components which are amplified. For such conditions the FBP needs to be accompanied by a low-pass filter to filter the noise e.g. the Butterworth (Gilland et al., 1988), Hann or Parzen filters (English et al., 1988). The filter may either be applied to each projection or after reconstruction on each transaxial slice. The former case is preferred to avoid reconstruction with noise in this study.

Inherent limitations of the FBP reconstruction are aliasing and the Gibbs phenomenon.

Aliasing occurs due to the loss of high spatial frequencies when the projection is sampled or digitised. The effect is noticeable when sharp boundaries that are rich in high frequencies are present. The Gibbs phenomenon is the ringing effect due to the cut-off frequency at sharp boundaries. Interpolation is required in FBP during the back-projection. Approximate interpolation is used with FBP to increase the speed of the algorithm. The interpolation errors can result in loss of spatial resolution, and streaking artefacts at sharp edges (Brooks and Di Chiro et al., 1976).

The FBP may provide accurate reconstruction. However when the FBP algorithm is applied directly to projection data acquired using a SPECT system, the reconstructed image will be limited in terms of accurate quantification, spatial resolution and contrast while image artefacts and distortion also may result (Tsui et al, 1994a).

2.5.3 Iterative reconstruction algorithms

The iterative approach is based on the process of matching the measured projection to the calculated projection (Zaidi, 1996). Iterative algorithms estimate the distributions through successive approximations. A brief discussion of some of the reconstruction techniques will be given.

Iterative reconstruction techniques are useful to reduce artefacts, especially in the low-count regions adjacent to high-count structures (Miller et al., 1997) or when the signal-to-noise ratio is low. Iterative reconstruction algorithms can be divided into two broad classes i.e. iterative filtered back-projection and statistical reconstruction algorithms (Galt et al., 1999).

2.5.3.1 Iterative Filtered Back-Projection algorithms

The iterative filtered back-projection (IFBP) algorithms are based on Chang's method (Chang, 1978) and they are useful for the reconstruction of attenuation maps and reconstruction of emission data with attenuation correction maps. In brief, these algorithms start with an estimate of the transverse image such as from FBP reconstruction or a uniform image, and model the emission acquisition process to form a new set of projections. These projections are compared with measured images and the results are used to improve the initial state (Miles et al., 1999).

When the projected estimator approximates the measured images with a pre-determined accuracy, the process is said to have converged. However with IFBP, the convergency is not well defined mathematically. The major advantage of IFBP algorithms is that all known distortions during acquisition can be modelled and included in the projection matrix and thus can be corrected for during reconstruction (Blokland et al., 1992). However too many iterations can amplify noise and degrade the image quality (Miles et al., 1999). IFBP algorithms have the potential to improve the diagnostic accuracy of cardiac SPECT with attenuation correction (Cullom et al., 1987). The major problem associated with this algorithm is an enormous amount of data that must be processed (Blokland et al., 1992).

2.5.3.2 Statistical reconstruction algorithms

These algorithms are based on the probability of photon interactions and detection given attenuation and other physical factors. They attempt to reconstruct the images based on the quantitative criteria they are optimising (Tsui et al., 1989; Tung et al, 1992). These

algorithms also require an image model for the re-projection data that can incorporate physical factors affecting the accuracy of the projections such as attenuation, Compton scattering, the statistics of radioactive decay and variable spatial resolution (Zeng et al., 1991; Tsui et al, 1988)

Maximum likelihood expectation maximisation (ML-EM) (Tsui et al, 1989) is an example of a statistical reconstruction algorithm. The ML-EM algorithm attempted to determine the tracer distribution that would most likely yield the measured projection given the imaging model and attenuation map.

The ML-EM algorithm could be used to accurately reconstruct Nuclear Medicine images because it models the noise variations and has been shown to improve performance compared with the FBP in the presence of noise. However ML-EM algorithm may limit image contrast (Miles et al, 1999). The ML-EM algorithm converged slowly, and therefore it required more iterations which resulted susceptibility to noise (Tsui et al., 1989). The points of convergence of this algorithm and the related number of iterations for clinical use have been a source of debate (Snyder et al, 1987). There is no common rule for stopping the algorithm after an optimal number of iterations on clinical data (Galt et al, 1999).

2.5.3.2.1 Mathematical framework

Let $f(x,y)$ be the true distribution of activity that is approximated by an array of cells of uniform distribution as illustrated in *figure 2.5*. The image (radioactive distribution) is defined to be a vector X i.e. $X = \{x_j: j= 1, \dots, N\}$. The distribution in the j^{th} cell is called x_j and N is the total number of cells in the image. The discrete function that has to be

solved is given by:

$$p_i = \sum_{j=1}^N c_{ij} x_j \quad 2.8$$

where c_{ij} is the weighting factor that represents the contribution of the j^{th} cell to the i^{th} projection, p_i ($i = 1 \dots M$) with M the number of projections. The weighting factor models the projection operation that can include all known distortions, for example scatter, attenuation and depth-dependent resolution.

Equation 2.8 can also be written in matrix format with C a weighting factor and P the projection matrix as:

$$P = CX \quad 2.9$$

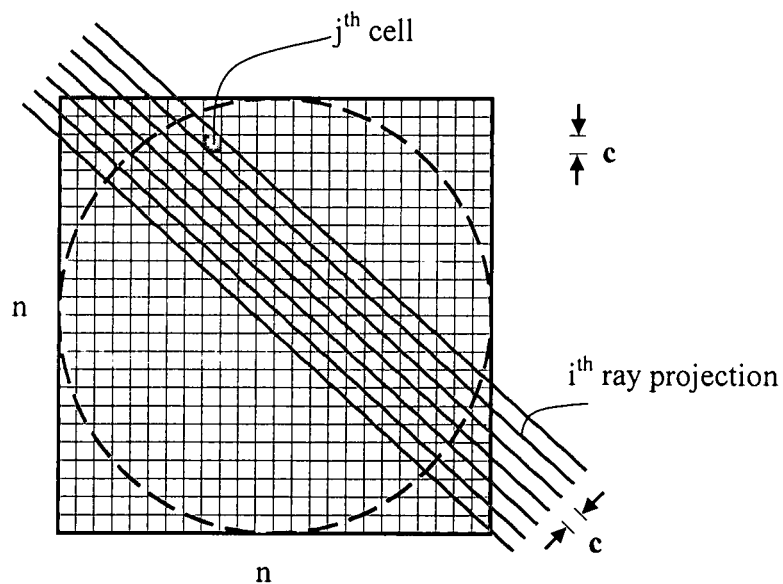


Figure 2.5: Square array used for iterative reconstructions.

The basic strategy of iterative methods is to apply corrections to arbitrary initial cell densities in an attempt to match the measured ray projections. Since former matching is

lost as new corrections are made, the procedure is repeated until the calculated projections agree with the measured ones to within the desired accuracy. The number of iterations limits the accuracy (Brooks and Di Chiro, 1976).

2.5.3.2.2 Expectation maximisation algorithm

The 'measured' data set was used in combination with a postulated, 'complete' data set in the expectation maximisation (EM) algorithm to facilitate the process of maximising the likelihood function of the measured data. The approach on calculation consisted of a series of alternating expectation steps and maximisation steps. This iterative process was theoretically equivalent to the original task of maximising the likelihood function defined on the measured data.

The EM algorithm was based on the Poisson model, which accurately modelled low count data (Dempster *et al*, 1977). To understand the algorithm, it is necessary to deal with the basic statistical background.

2.5.3.2.3 Statistical Background

Suppose that a long-lived radioactive sample is counted repeatedly under supposedly identical conditions with a properly operating system. The disintegration of the radioactive sample is a random process from one moment to another and the probability of the process taking place has to be considered (Sorenson and Phelps, 1987). Such an experiment is an experiment of chance (random) events associated with a probabilistic model. Let a *random variable*, say X , be a function defined over a sample space. If the set of all possible outcomes from a *random variable* X is a countable set, $x_1, x_2, x_3, \dots, x_n$ then

X is called a discrete random variable, (Bain and Engelhardt, 1987).

This random variable, X , can be described by the discrete density function:

$$f(x) = P[X = x] \quad x = x_1, x_2, \dots \quad 2.10$$

with such properties

$$0 \leq f(x_i) \leq 1 \quad 2.11$$

$$\sum_{i=1}^n f(x_i) = 1 \quad 2.12$$

Typical discrete random variables are integer values and the event cannot overlap because only one value X is assigned to each sample point (Berger, 1992). The discrete density function provides a model for a theoretical frequency distribution of a random variable and hence must possess a mean, variance, standard deviation and other descriptive measures associated with the theoretical population that it represents.

2.5.3.2.4 Expectation Maximisation Reconstruction Algorithm

Let us assume the measured data in an experiment is a random vector $Y = Y_1, Y_2, \dots, Y_M$. Y_i is the total number of counts in the i^{th} projection and M the number of projections. The EM algorithm now postulates a 'complete data' random vector X such that Y is a function of X .

The notation used by Lange and Carson (1984) will be used in this short discussion of the EM algorithm and is as follows:

- i : projection subscript
 j : pixel subscript ($j = 1, \dots, N$)
 I_i : set of pixels contributing to projection I
 J_j : set of projections to which pixel j contributes
 θ_j : source intensity of pixel j
 b_{ij} : probability that a photon leaving pixel j reaches the i^{th} projection

Let $X_{ij}, j \in I_i$ be the complete (unobserved) number of photons originating randomly from pixel j in a direction perpendicular to the scintillation camera contributing to projection i . X_{ij} is a complete set of data. The average of X_{ij} can be defined as $c_{ij}\theta_j$. The parameters c_{ij} will be considered to be known constants and the intensities θ_j have to be estimated. The total number of photons recorded in a projection i is given by Y_i and shown in equation 2.13.

$$Y_i = \sum_{j \in I_i} X_{ij} \quad 2.13$$

X_{ij} and Y_i obey the Poisson distributions. Y_i are the observed data for projection i . X_{ij} constitutes the unobserved but complete data.

The new estimate (Lange and Carson, 1994) is given by:

$$\theta_j^{n+1} = \frac{\theta_j^n}{\sum_{i \in J_j} c_{ij}} \sum_{i \in J_j} \frac{c_{ij} Y_i}{\sum_{k \in I_i} c_{ik} \theta_k^n} \quad 2.14$$

for component j of the new parameter θ^{n+1} . This estimated number is set equal to the expected number of photons $\sum_j c_{ij}\theta_j$ and the resulting equation is solved for θ_j .

The initial estimate θ^0 is usually set to be a uniform source distribution with non-negative values. Convergence of the estimates obtained in *equation 2.14* and convergence to the maximum likelihood (ML) estimate has been demonstrated (Shepp and Vardi, 1982; Lange and Carson, 1984). If a non-negative initial estimate is chosen, it is obvious from *equation 2.14* that all images produced in subsequent iterations remain non-negative. This guarantees that negative pixel values, which are physically impossible, will not be produced.

It can be verified at each iteration that:

$$\sum_i \sum_{j \in I_i} c_{ij} \theta_j^n = \sum_i Y_i \quad 2.15$$

This implies that the total number of events at each iteration is equal to the sum of the measured data.

The low convergence rate and computational burden are the major disadvantages of EM reconstruction algorithms. To remedy the drawback of convergence especially for clinical purposes, it was possible to incorporate acceleration schemes to achieve a faster rate of increase of the likelihood function at each iteration.

2.5.4 Accelerated iterative techniques.

2.5.4.1 Introduction

The EM algorithm was used to compensate for physical distortions and accounts for the statistical nature of radioactive disintegration and to produce high quality reconstruction. Unfortunately EM is computer intensive, and convergence is slow. Some investigators applied acceleration techniques to improve the convergence speed.

The computational time of the ML-EM algorithm is too long to be clinically feasible (Dey et al., 1998). The approach of ordering the projection data has been suggested for speeding up the reconstruction process (Hudson and Larkin, 1994). It was also possible to use only a subset of available projection angles at each iteration, thus achieving a reduction in computational time (Chen et al., 1988; Tanaka, 1987). The approach of using an initial estimate that is better than the uniform distribution in the sense of a greater likelihood, could also improve computational efficiency (Snyder et al., 1987).

Murase *et al.* (1994) compared three different accelerated iterative reconstruction techniques. These techniques were the filtered iterative reconstruction (Tanaka et al., 1987), accelerated expectation maximisation algorithm using multiplicative correction and the one using an additive correction technique (Chen *et al.*, 1988). The method proposed by Tanaka et al. (1987) was a modification to the ML-EM algorithm. This algorithm enhanced the high frequency components and resulted in significantly improved frequency response. Acceptable images were obtained with as few as two to five iterations. In the interest of convergency, this has the fastest convergency and thus requires fewer iterations for acceptable results. However, this method still takes 50 – 100

times longer than filtered back-projection and is considered too tedious for application in daily clinical practice.

Hudson and Larkin (1994) have proposed an algorithm called the ordered subset expectation maximisation (OSEM). This algorithm selected subsets of the data and then applied the EM algorithm sequentially to each subset. The use of subsets in the iterative steps of reconstruction speeded up the reconstruction process (Galt *et al.*, 1999). If, for example, 32 subsets were selected, the algorithm provided similar convergence and noise results in 1 iteration as 32 iterations of the standard EM algorithm would have done.

Dey *et al.* (1998) found that although the Chang and OSEM methods were comparable in calculation time, the OSEM reconstruction method gave a more accurate activity distribution.

2.5.4.2 Ordered Subsets Expectation Maximisation Reconstruction algorithm

The OSEM proposed by Hudson and Larkin (1994) resulted in images essentially identical to those from non-accelerated EM with an improvement in speed and a one tenth reduction in the number of iterations (Manglos *et al.*, 1995). The ordering of the subsets in the OSEM speeded up the reconstruction process. For example, if images are acquired in a 64 x 64 matrix with 64 projections a subset of 32 can be chosen. This implied that each subset would consist of two projections and therefore would result in a total of 128 (2 x 64) projection rays. The standard EM-algorithm was then applied to each of the subsets in turn using the rows of the designed matrix corresponding to these ray sums. The resulting reconstruction becomes the starting value of the next subset. An iteration of the OSEM was a single pass through all the specified subsets. More iterations

could be performed by using the result of the previous iteration as starting point for the following iteration.

2.5.4.3 Selection of subsets and order of reconstruction.

Hudson and Larkin (1994) reported that it was best to order the subsets such that the projections were chosen which corresponded to angles with maximum angular distance from those previously used. They were chosen at each step and the order in which projections were processed was arbitrary. This arbitrary order selection accelerated convergence as compared to random or sequential ordering of the subsets. Ordering of pairs was orthogonal as, $\{\Theta^\circ, \Theta+180^\circ\}$ for example a typical subset will be $\{(0^\circ, 180^\circ); (90^\circ, 270^\circ); (45^\circ, 225^\circ); (135^\circ, 315^\circ); (22.5^\circ, 202.5^\circ); (11.25^\circ, 191.25^\circ); (67.5^\circ, 247.5^\circ)\dots\}$.

An assumption for the use of OSEM reconstruction was that there will be subset balance, i.e. the sum of counts in projections forming each subset should be equal (Hutton and Lau, 1997). In mathematical cardiac torso (MCAT) phantom studies, Hutton and Lau (1997) reported that a significant loss of subset balance occurred when a subset size of two was used with the OSEM algorithm. They suggested from their results that the subset balance was sufficiently good provided at least four projections per subset were used for 360° tomography.

The comparison of sequential and orthogonal ordering by Manglos et al. (1995) suggested that the subset ordering (as opposed to the subset size) was unimportant in

determining the convergence rate of OSEM. However Li et al. (1994), using an emission rather than transmission algorithm, reported a substantial improvement with orthogonal ordering compared to sequential ordering.

2.5.5 Separable paraboloidal surrogate reconstruction

The OSEM algorithm proposed by Larkin and Hudson (1994) has been used as an accurate method for emission and transmission image reconstruction. It is used in clinical studies because of the acceleration of the original EM algorithm, the ease in programming and the high quality images obtained after a few iterations. Although the images may look good, variance and resolution properties of OSEM are not clear and this algorithm does not converge (Erdoğan and Fessler, 1999).

The separable paraboloidal surrogate (SPS) reconstruction proposed by Erdoğan and Fessler (1999) has some advantages over OSEM. It was guaranteed to be monotonically even with non-zero background events. It was not only derived from the ML problem but also from the penalised likelihood (PL), which had a better quality of the image reconstruction than the ML (Erdoğan and Fessler, 1999).

Although the OSEM accelerated the original transmission ML algorithm, the convergence was still slow. Nuyts et al. (1998) found that the OSEM method disregarded the background counts.

The idea of ordered subset could also be applied to SPS because of the ordered subset advantage mentioned previously. The ordered subset of SPS was referred to as ordered subset transmission (OSTR) (Erdoğan and Fessler, 1999).

Phantom studies using positron emission tomography (PET) showed that the results based on PL reconstructed images were better than the results from the ML methods. ML for OSTR was also superior to OSEM. Therefore ML-OSTR and PL-OSTR are considered better than OSEM. OSTR was easy to implement with any type of the system and offered faster convergence than OSEM (Erdoğan and Fessler, 1999). Although the phantom studies were done on the PET system, it was reported that the algorithm was useful also for SPECT and x-ray CT (Erdoğan and Fessler, 1999).

2.6 Discussion

Quantification of the 3D activity distribution inside the patient is becoming the major goal in SPECT. Due to the random nature of photon emission detection, SPECT projections are noisy and are physically distorted by attenuation, scatter from the surrounding tissues and gamma camera resolution.

Attenuation correction techniques needed to account for inhomogeneity and preferably fast-processing algorithms should be used. The most effective method was to use an iterative method with an attenuation coefficient map obtained from transmission data.

The poor resolution of the NaI (Tl) crystal used in gamma camera systems makes it difficult to discriminate all scattered photons from primary photons. A technique that discriminates most of the scattered photons and does not require pre-calibration was needed. The TEW technique was the method of choice for scatter compensation because was efficient and easy to use.

Reconstruction algorithms that account for the above-mentioned problems need to be considered for processing of SPECT images. Filtered back-projection algorithms in SPECT are based on the back-projection of filtered projections. Although they provide speed, they are limited by sub-optimal use of statistical information and by ignoring physical factors such as photon attenuation and scatter.

Iterative reconstruction algorithms are based on the statistical nature of the SPECT photon detection process and they can correct for attenuation, Compton scattering of photons and gamma camera resolution variation. Such algorithms are processor intensive because enormous amounts of data have to be processed. Developments in computer technology should result in faster theoretical algorithms.

ML-EM algorithms are iterative reconstruction algorithms based on maximum likelihood estimation. They are less sensitive to noise and give accurate results. However they have the disadvantages of slow convergence and high amount of data to be processed.

OSEM was used in this study as it is the combination of ML-EM with fast iterative techniques ordering the subsets of the projections facilitated processing of data.

References

- Almeida P, Bendriem B, de Dreuille O, Peltier A, Perrot C, Brulon V (1998). Dosimetry of transmission measurements in nuclear medicine: A study using anthropomorphic phantoms and thermoluminescent dosimeters. *Eur J Nucl Med*; 25: pp1435 – 1441.
- Almquist H, Palmer J, Ljungberg M, Wollmer P, Strand S-E, Jonson B (1990). Quantitative SPECT by attenuation correction of the projection set using transmission data: Evaluation of a method. *Eur J Nucl Med*; 16: pp587 – 594.
- Appledorn CR (1989). An analytic solution to the nonstationary reconstruction problem in SPECT. *Proceedings of the 1989 international conference on information processing in medical imaging*; 36: pp69 – 79
- Axelsson B, Msaki P, Israelsson A (1984). Subtraction of Compton-scattered photons in single-photon emission computerized tomography. *J Nucl Med*; 25: pp490 – 494.
- Bailey DL, Hutton BF, Walker PJ (1987). Improved SPECT using simultaneous emission and transmission tomography. *J Nucl Med*; 28: pp844 – 851.
- Bain LJ, Engelhardt M (1987). *Introduction to probability and mathematical statistics*. Duxbury Press, Boston. pp262 – 308.
- Beck RN, Zimmer LT, Charleston DB (1973). Advances in fundamental aspects of imaging system and techniques, In *Medical Radioisotope Scanning*. Vienna; IAEA: 1, pp3-45
- Beekman F, Eijkman EM, Viergever M *et al* (1993). Object shape dependent PSF model for SPECT imaging. *IEEE Trans Nucl Sci*; NS-40: pp31 – 39.
- Beekman FJ, Kamphuis C, Hutton BF, van Rijk PP (1998). Half-beam collimators combined with scanning point source for simultaneous emission-transmission imaging. *J Nucl Med*; 39:pp1996-2003
- Berger MA (1992). An introduction to probability and stochastic process. *Springer-Verlag*, New York. pp1-2
- Blokland JAK, Reiber JHC, Pauwels EKJ (1992). Quantitative analysis in single photon emission tomography (SPET). *Eur J Nucl Med*; 19: pp47 – 61.
- Brooks RA, Di Chiro G (1976). Principles of computer assisted tomography (CAT) in radiographic and radioisotopic imaging. *Phys Med Biol*; 21: pp689 – 732

- Buvat I, Rodrigues-Villafuerte M, Todd-Pokropek A, Benali H, Di Paola R (1995). Comparative assessment of nine scatter correction methods based on spectral analysis using Monte Carlo simulation. *J Nucl Med*; 36: pp1476 – 1488.
- Chang LT (1978). A method for attenuation correction in radionuclide computed tomography. *IEEE Trans Nucl Sci*; NS-25: pp638 – 643.
- Chang LT, Loncaric S, Huang G, Sanpitak P (1995). A symmetric fan transmission CT on SPECT to derive μ -maps for attenuation correction. *Phys Med Biol*; 40: pp913 – 928.
- Chen C-T, Metz CE, Hu Xiaoping Hu (1988). Maximum likelihood reconstruction in PET and TOFPET. In: *Mathematics and computer science in medical imaging*. Edited by Viergever MA, Todd-Pokropek A. Springer-Verlag, Berlin, Heidelberg, Germany
- Chornoboy ES, Chen CJ, Miller MI, Miller TR, Snyder DL (1990). An evaluation of maximum likelihood reconstruction for SPECT. *IEEE Trans Med Imag*; 9: pp99–110.
- Corbet JR, Ficaro EP (1999). Clinical review of attenuation-corrected cardiac SPECT. *J Nucl Card*; 6: pp54 – 68.
- Cullom SJ, Hendel RC, Liu L, Garcia EV, White ML, Kiat H, Berman DS (1996). Diagnostic accuracy and image quality of a scatter attenuation and resolution compensation method for Tc-99m-sestamibi cardiac SPECT. *J Nucl Med*; 37: p81P.
- Curry III T, Dowdey JE, Murry Jr RC (1990). *Christensen's physics of diagnostic radiology* 4th edition, Lea and Febiger, Philadelphia, USA: pp 70 - 80
- Dempster AP, Laird NM, Rubin DB (1977). Maximum likelihood from incomplete data via the EM algorithm. *J. Royal Statist. Soc., B*; 39:1: pp 1–37.
- De Puey EG, Garcia EV (1989). Optimal specificity of thallium-201 SPECT through recognition of imaging artefact, *J Nucl Med*; 30: pp441–449.
- De Puey EG (1994). How to detect and avoid myocardial perfusion SPECT artefacts, *J Nucl Med*; 35: pp699–702.
- Dey D, Slomka PJ, Hahn LJ, Kloiber R (1998). Comparison of ordered subsets expectation maximization and Chang's attenuation correction method in quantitative cardiac SPET: A phantom study. *Nucl Med Comm*; 19: pp1149 – 1157.
- Du Raan H, du Toit PD, van Aswegen A, MG Lötter, Herbst CP, van der Walt TN, Otto AC (2000). Implementation of a Tc-99m and Ce-139 scanning line source for attenuation correction in SPECT using a dual opposing detector scintillation system. *Med Phys*; 27: pp 1523 – 1534.
- English RJ, Brown SE (1988). *SPECT: Single photon emission computed tomography: a*

primer 2nd edition, The society of Nuclear Medicine, New York, NY. pp89 – 94.

Erdoğan H, Fessler JA (1999). Ordered subsets algorithms for transmission tomography. *Phys Med Biol*; 44: pp2835 – 2851.

Ficaro EP, Fessler JA, Rogers WL, Schwaiger M (1994). Comparison of Americium-241 and Technetium-99m sources for attenuation correction of Thallium-201 SPECT imaging of the heart. *J Nucl Med*; 35: pp652 – 663.

Floyd CE, Jaszczak RJ, Greer KL, Coleman RE (1985): Deconvolution of Compton scatter in SPECT. *J Nucl Med*; 26: pp403 – 408.

Frey EC, Tsui BMW, Perry JR (1992). Simultaneous acquisition of emission and transmission data for improved Thallium-201 cardiac SPECT imaging using a Technetium-99m transmission source. *J Nucl Med*; 33: pp2238 – 2245.

Frey EC, Tsui BMW (1994). Modelling the scatter response function in inhomogeneous scattering media for SPECT. *IEEE Trans Nucl Sci*; 41: pp1585 – 1593.

Galt JR, Cullom SJ, Garcia EV (1999). Attenuation and scatter compensation in myocardial perfusion SPECT. *Seminars in Nuclear Medicine*; XXIX, pp204 – 220

Gilland DR, Tsui BMW, McCartney WH, Perry JR (1988). Determination of the optimum filter function for SPECT imaging. *J Nucl Med*; 29: pp643 – 650.

Gregoriou GK, Tsui BMW, Gullberg GT (1998). Evaluation of the effect on myocardial defect detection in truncated and nontruncated fanbeam attenuation compensation SPECT images using observer performance and ROC studies. *J Nucl Med*; 39: pp166 – 175.

Gullberg GT (1998). Innovative design concepts for transmission CT in attenuation-corrected SPECT imaging. *J Nucl Med*; 39: pp1344 – 1347.

Harris CC, Greer KL, Jaszczak RJ, Floyd CE, Fearnow EC, Coleman RE (1984). ^{99m}Tc attenuation coefficients in water-filled phantoms determined with gamma cameras. *Med Phys*; 11: pp681 – 685.

Hashimoto J, Kubo A, Ogawa K, Amano T, Fukuuchi Y, Nobutoku M, Ichihara T (1997). Scatter and attenuation correction in Technetium-99m Brain SPECT. *J Nucl Med*; 38: pp157 – 162.

Hashimoto J, Sasaki T, Ogawa K, Kubo A, Motomura N, Ichihara T, Amano T, Fukuuchi Y (1999). Effect of the scatter and attenuation correction on quantitative analysis of β -CIT brain SPET. *Nucl Med Comm*; 20: pp159 – 165.

Hawman EG, Ficaro EP, Hamill JJ, Schwaiger M (1994). Fan beam collimation with off centre focus for simultaneous emission/ transmission SPECT in multicamera SPECT

system. *J Nucl Med*; 35: 92P

Hendee WR (1984), *Medical radiation physics 2nd edition*, Yearbook medical publishers Inc, Chicago, USA: pp 379 – 381.

Hudson HM, Larkin RS (1994). Accelerated image reconstruction using ordered subsets of projection data. *IEEE Trans Med Imag*; 20: pp100 – 108.

Hutton BF, Lau YH (1997). How critical is subset balance for OSEM reconstruction in myocardial SPECT? *J Nucl Med*; 38, Suppl, p57P.

Ichihara T, Ogawa K, Motomura N, Kubo A, Hashimoto S (1993). Compton scatter compensation using the Triple-Energy Window method for single- and dual-isotope SPECT. *J Nucl Med*; 34: pp2216 – 2221.

ICRU Report 44 (1989). Tissue substitutes in radiation dosimetry and measurement.

Jaszczak RJ, Gilland DR, Hanson MW, Jang S, Greer KL, Coleman RE (1993). Fast transmission CT for determining attenuation maps using a collimated line source, rotatable air-copper-lead attenuators and fan-beam collimation. *J Nucl Med*; 34: pp1577 – 1586.

Jaszczak RJ, Greer KL, Floyd CE, Harris CC, Coleman RE (1984). Improved SPECT quantification using compensation for scattered photons. *J Nucl Med*; 25: pp893 – 900.

Kadrmas DJ, Frey EC, Tsui BMW (1998). Application of reconstruction-based scatter compensation to thallium-201 SPECT: Implementations of reduced reconstructed image noise. *IEEE Trans Nucl Sci*; 17: pp325 – 333.

King MA, Doherty PW, Schringer RB (1983): A Weiner filter for nuclear medicine images. *Med Phys*; 10: pp876 – 880.

King MA, Coleman M, Penney BC, Glick SJ (1991): Activity quantitation in SPECT: A study of prereconstruction Metz filtering and the use of scatter degradation factor. *Med Phys*; 18: pp184 – 189.

King MA, Hademenos GJ, Glick SJ (1992). A dual-photo peak window method for scatter correction. *J Nucl Med*; 33: pp605 – 612.

King MA, Tsui BMW, Pan TS (1995). Attenuation compensation for cardiac single photon emission computed tomographic imaging: Impact of attenuation and methods of estimating attenuation maps. *J Nucl Cardiol*; 2: pp513 – 524.

King MA, Luo D, Dahlberg S, Penney B, Morgan H (1996). Transmission imaging of large attenuators using a slant hole collimator on a three-head SPECT system. *Med Phys*; 23: pp263 – 272.

- Knesaurek K, King MA, Glick SJ (1989). Investigation of causes of geometric distortion in 180 degree and 360 degree angular sampling in SPECT. *J Nucl Med*; 30: pp 1666 – 1675.
- Koral KF, Wang X, Rogers WL, Clinthorne NH (1988). SPECT Compton-scattering correction by analysis of energy spectra. *J Nucl Med*; 30: pp195-202.
- Koral KF, Fayez MS, Buchbinder S, Clinthorne NH, Rogers WL, Tsui BMW (1990). SPECT dual energy window Compton correction: Scatter multiplier required for quantification. *J Nucl Med*; 31: pp90 – 98.
- Lange K, Carson R (1984). EM reconstruction algorithms for emission and transmission tomography. *J Comput Assist Tomogr*; 8: pp306 – 316.
- Larson LA (1980). Gamma camera emission tomography. *Acta Radiol*; 363: pp1 – 80.
- Li J, Jaszczak RJ, Greer KL, Coleman RE (1994). Implementation of an accelerated iterative algorithm for cone-beam SPECT. *Phys Med Biol*; 39: pp643 – 653.
- Liang Z (1993). Compensation for attenuation, scatter, and detector response in SPECT reconstruction via iterative FBP methods. *Med Phys*; 20: pp1 – 10.
- Ljungberg M, King MA, Hademenos GJ, Strand S-E (1994). Comparison of four scatter correction methods using Monte Carlo simulated source distributions. *J Nucl Med*; 35: pp143 – 151.
- Madsen MT, Kirchner PT, Grover-McKay M, Aktay R, Seabold JS, Rezai K, Kelly G (1997). Emission based attenuation correction of myocardial perfusion studies. *J Nucl Med*; 4: pp477 – 486.
- Maniawski PJ, Morgan HT, Wackers FJT (1991). Orbit-related variation in spatial resolution as a source of artefactual defects in Thallium-201 SPECT. *J Nucl Med*; 32: pp871 – 875.
- Manglos SH, Gagne GM, Krol A, Thomas FD, Narayanaswamy R (1995). Transmission maximum-likelihood reconstruction with ordered subsets for cone beam CT. *Phys Med Biol*; 40: pp1225 – 1241.
- Matsunari I, Boning G, Ziegler S I, Kosa I, Nekolla SG, Ficaro EP, Schwaiger M (1998). Effects of Misalignment between transmission and emission scans on attenuation corrected cardiac SPECT. *J Nucl Med*; 39, pp411 – 416.
- Metz CE (1969). A mathematical investigation of radioisotope scan imaging processing. *PhD thesis*. University of Pennsylvania. USA.

- Miles J, Cullom J, Case A (1999). An introduction to attenuation correction. *J Nucl Cardiol*; 6: pp449 – 457.
- Miller TR, Wallis JW, Dai G, Miller MM (1997). Iterative reconstruction algorithms: Their clinical value. *J Nucl Med*; 38, Suppl, p222P.
- Murase K, Tanada S, Sugawara Y, Tauxa WN, Hamamoto K (1994). An evaluation of the accelerated expectation maximization algorithms for single-photon emission tomography image reconstruction. *Eur J Nucl Med*; 21: pp 597 – 603.
- Naudé H, Van Aswegen A, Herbst CP, Lötter MG, Pretorius PH (1996). A Monte Carlo evaluation of the channel ratio scatter correction. *Phys Med Biol*; 41, Supplement, p1058-1066.
- Naudé H, Van Aswegen A, Lötter MG, Du Toit PD, Pretorius PH, Herbst CP. (1997). Implementation of a scanning line source (Tc-99m & Ce-139) for attenuation correction in SPECT using a dual opposing head scintillation camera. *J Nucl Med*; 38, Supplement, p217P.
- Naudé H (1998). Scatter and attenuation correction techniques for absolute quantification of radionuclide distributions with SPECT. *PhD Thesis*, UOVS, Bloemfontein.
- Nuyts J, Man BD, Dupont P, Defrise M, Suetens P, Mortelmans L (1998). Iterative reconstruction for helical CT simulation study. *Phys Med Biol*; 40: pp1225 – 1241.
- Ogasawara K, Hashimoto J, Ogawa K, Kubo A, Motomura N, Hasegawa H, Ichihara T (1998). Simultaneous acquisition of Iodine-123 and Technetium-99m transmission data for quantitative brain single-photon emission tomographic imaging. *J Nucl Med*; 25: pp1537 – 1544.
- Ogawa K, Harata Y, Ichihara T, Kubo A, Hashimoto S (1990). Estimation of scatter component in SPECT planar image using a Monte Carlo method. *Jpn J Nucl Med*; 27: pp467 – 475.
- Ogawa K, Harata Y, Ichihara T, Kubo A, Hashimoto S (1991). A practical method for position-dependent Compton-scatter correction in single photon emission CT. *IEEE Trans Med Imag*; 10: pp408 – 412.
- Pan TS, Metz CE, Chen CT (1997). Non-iterative methods and their noise characteristics in 2D SPECT image reconstruction. *IEEE Trans Med Nucl Sci*; 44: pp1388 – 1397.
- Pretorius PH, AJ van Rensburg, van Aswegen A, Lötter MG, Serfontein DE, Herbst CP (1993). The channel ratio method of scatter correction for radionuclide image quantitation. *J Nucl Med*; 34: pp330 – 335.
- Shepp LA, Vardi Y (1982). Maximum likelihood reconstruction for emission

tomography. *IEEE Trans Med Imag*; MI-1: pp113 – 122.

Snyder DL, Miller MI, Thomas LJ Jr, Politte DG (1987). Noise and edge artefact in maximum likelihood reconstruction for emission tomography. *IEEE Trans Med Imag*; MI-6: pp228 – 238.

Sorenson JA (1984). Quantitative measurement of radiation *in vivo* by whole body counting, In Hine GH, Sorenson JA (eds): *Instruments in Nuclear Medicine*, vol 2. New York, NY, Academic, pp 311-349.

Sorenson JA, Phelps ME (1987). Image quality in Nuclear Medicine. In: *Physics in Nuclear Medicine*, 2nd edition; WB Saunders Company, Philadelphia, pp362-366.

Tan P, Bailey DL, Meikle SR, Eberl S, Fulton RR, Hutton BF (1993). A scanning line source for simultaneous emission and transmission measurements in SPECT. *J Nucl Med*; 34: pp1752 – 1760.

Tanaka E (1983). Quantitative image reconstruction with weighted back projection for single photon emission computed tomography. *J Comp Asst Tomogr*; 17: pp692 – 699.

Tanaka E (1987). A fast reconstruction algorithm for stationary positron emission tomography based on a modified EM algorithm. *IEEE Trans Med Im*; MI-6: pp98 –105.

Tsui BMW, Hu H, Gilland DR, Gullberg GT (1988). Implementation of simultaneous attenuation and detector response correction in SPECT. *IEEE Trans Nucl Sci*; 35: pp778 – 783.

Tsui BMW, Gullberg GT, Edgerton ER, Ballard JG, Perry JR, McCartney WH, Berg J (1989). Correction of nonuniform attenuation in cardiac SPECT imaging. *J Nucl Med*; 30: pp497 – 507.

Tsui BMW, Zhao X, Frey EC, McCartney WH (1994a). Quantitative Single- Photon Emission Computed Tomography: Basic and clinical consideration. *Seminars in Nuclear medicine*; XXIV: pp38 – 65.

Tsui BMW, Frey EC, Zhao X, Lalush DS, Johnston RE, McCartney WH (1994b). The importance and implementation of accurate 3D compensation methods for quantitative SPECT. *Phys Med Biol*; 39: pp509 – 530.

Tsui BMW, Frey EC, LaCroix KJ, Lalush DS, McCartney WH, King MA, Gullberg GT (1998). Quantitative myocardial perfusion SPECT. *J Nucl Cardiol*; 5: pp507 – 522.

Tung CH, Gullberg GT, Zeng GL, Christian PE, Datz FL, Morgan HT (1992). Non-uniform attenuation correction using simultaneous transmission and emission converging tomography. *IEEE Trans Nucl Sci*; 39: pp134 – 143.

Wang H, Jaszczak RJ, McCormick JW, Greer KL, Coleman RE (1995). Experimental evaluation of a Tellurium-123m transmission source to determine attenuation maps for SPECT. *IEEE Trans Nucl Sci*; 42: pp1214 – 1219.

Walters TE, Simon W, Chesler DA, Correlia JA (1981). Attenuation correction in gamma emission computed tomography: *J Comp Asst Tomogr*; 5, pp89 – 94.

Webb S (1988). *The physics of medical imaging*. Adam Hilger, London, UK, pp 221 – 226.

Welch A, Gullberg GT, Christian PE, Datz FL (1994). A comparison of Gd/Tc versus Tc/Tl simultaneous transmission and emission imaging using both single triple fan-beam SPECT systems. *IEEE Trans Nucl Sci*; 41: pp2779-2786.

Zaidi H (1996). Quantitative SPECT: Recent developments in detector response, attenuation and scatter compensation techniques. *Physica Medica*; XII (3): pp101 – 117.

Zeeberg BR, Bice AN, Loncaric S et al. (1987). A theoretical correct algorithm to compensate for a 3D spatially variant point spread function in SPECT imaging. Proceedings of the 1987 International Conference on Information Processing in Medical Imaging; 36: pp69 – 79.

Zeng GL, Gullberg GT, Tsui BMW, Terry JA (1991). Three dimensional iterative reconstruction algorithms with attenuation and geometric point response correction. *IEEE Trans Nucl Sci*; 38: pp693 – 702.

CHAPTER 3: PHANTOM STUDIES TO EVALUATE RECONSTRUCTION PARAMETERS FOR MYOCARDIAL PERFUSION IMAGING.

3.1 Introduction.....	3.1
3.2 Methods.....	3.1
3.2.1 Data acquisition	3.1
3.2.2 Data reconstruction.....	3.2
3.2.3 Data analysis	3.2
3.2.3.1 Spatial resolution	3.3
3.2.3.2 Noise	3.3
3.3 Results.....	3.4
3.3.1 Spatial resolution.....	3.4
3.3.2 Noise	3.5
3.4 Discussion	3.7
References	3.9

3.1 Introduction

An accurate reconstruction technique is necessary to obtain the relative or absolute quantification of radionuclide uptake in patients' organs. The ordered subset expectation maximisation (OSEM) iterative technique was chosen for this study due to the advantages discussed in Chapter 2. The image quality depends on the subset size and number of iterations when using the OSEM method. Hutton and Lau (1997) suggested that subset balance was sufficiently good provided that at least four projections per subset are used for 360 degrees data. Tsui et al. (1989), Miller and Wallis (1992) and Miles et al. (1999) have reported the enhancement of noise after a larger number of iterations.

The purpose therefore, of this part of the study was to investigate the number of iterations and subset size, which give optimal results in myocardial SPECT images. This was done by evaluating the influence of these parameters on spatial resolution and noise in a series of phantom studies.

3.2 Methods

3.2.1 Data acquisition

The phantom used in this study was a perspex cylinder of 220mm diameter and 200mm height, with an insert consisting of six fillable lucite cylindrical tubes. The cylinders were of diameter 15mm, 16mm, 25mm, 32mm, 41mm and 60mm, all of height 170mm. This phantom was originally manufactured in-house (Naudè, 1998) for the evaluation of attenuation and scatter correction techniques. The cylindrical inserts were suitable to evaluate the system resolution and noise in this study. The cylinders were filled with the same concentration of ^{99m}Tc (0,4MBq/ml). The cylindrical insert was inserted in the

perspex cylinder and the latter filled with water to simulate a uniform attenuation medium as shown in *figure 3.1* (Naudè, 1998).

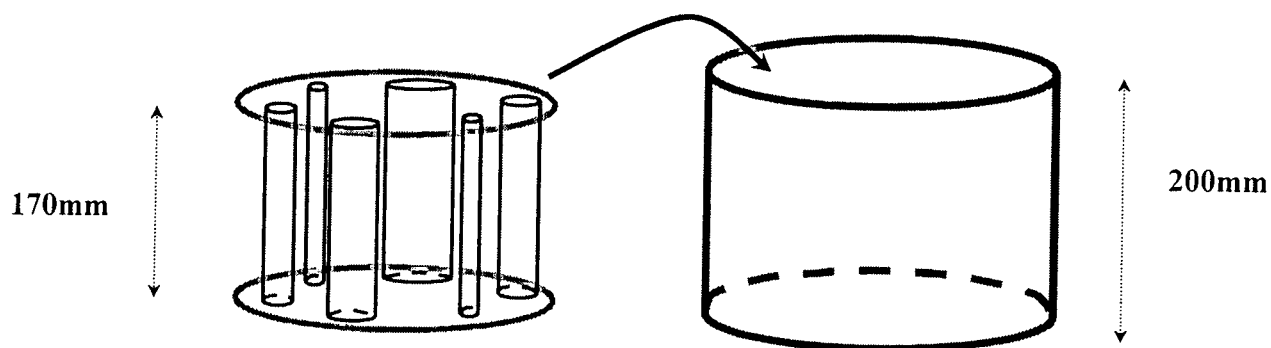


Figure 3.1: *The cylinder insert*

For this study, ^{99m}Tc was used as the emission source. The emission data were acquired through 360 degrees using a 128 x 128-word imaging matrix. This corresponds to a pixel size of 4.9mm. The detectors were equipped with LEHR collimators. The emission data were acquired in 64 projections, as used for clinical SPECT studies.

3.2.2 Data reconstruction

The emission data were smoothed using a 3x3 median filter and then reconstructed using the iterative OSEM reconstruction method. The OSEM method was applied using four different subset sizes (4, 8, 16 and 32) and a different number of iterations (1, 2, 5, 8 and 10) to yield twenty combinations of image data sets. A transaxial slice (1-pixel thick) was selected from the centre of each set of reconstructed data.

3.2.3 Data analysis

The twenty reconstructed images were compared to determine which subset and iteration

combination gave the best image quality. Image quality is determined by several factors such as spatial resolution, noise and contrast. These factors cannot be treated independently because improvement in one could result in the degradation of the other (Sorenson and Phelps, 1987). In this study the spatial resolution and noise were used to evaluate the image quality resulting from the different subsets and iterations.

3.2.3.1 Spatial resolution

Spatial resolution refers to the sharpness or detail of the image. Spatial resolution is determined by collimator resolution and intrinsic resolution. The quantitative approach used to evaluate the spatial resolution was the line spread function (LSF), which is the count rate profile of a point or line source across the reconstructed transverse image slice containing the radioactivity. Linear interpolations of the profile data were performed and the maximum in the profile was obtained. The full-width at half-maximum (FWHM) and full-width at tenth maximum (FWTM) values were used to calculate the LSF (Sorenson and Phelps, 1987).

Although each image represented contained six cylindrical inserts, FWHM and FWTM values were evaluated for only three of the smaller insert diameters (32mm, 25mm and 16mm) to evaluate system resolution.

3.2.3.2 Noise

Image noise may be either random or structured. Random noise can be caused by random statistical variation in the count rate, while structured noise refers to non-random variations in count rate superimposed on and interfering with the perception of the object

structure of interest. Random noise is related directly to the number of counts recorded per unit area of the image. Scintigraphic images may have excessive random noise as a result of low radiation source intensities or inefficient utilisation of emitted radiation (Sorenson and Phelps, 1987).

For each transaxial slice a circular region of interest (ROI) was drawn in the centre of the largest cylinder insert (diameter 60mm). The mean and standard deviation of the counts in the ROI were calculated. The noise in the image was calculated as the ratio of the standard deviation of the counts to the mean count and expressed as a percentage.

3.3 Results

3.3.1 Spatial resolution

The FWHM and FWTM values of the 32mm, 25mm and 16mm insert cylinders for the different subset and iteration combinations (Subset_iterations) used are listed in *table 3.1*. The results for the 32mm insert showed that the FWHM for 32 subsets decreased with the number of iterations. That was in contrast to results from 16, 8 and 4 subsets that generally increased with the number of iterations. The results from 4 subsets showed an initial decrease and increased further on. However, the FWTM for 32 subsets increased with the number of iterations and decreased for 16, 8 and 4 subsets. The FWHM and FWTM for 4 subsets showed the poorest spatial resolution.

For the 25mm cylindrical insert the FWHM for 16 and 8 subsets were very similar and did not vary much with number of iterations. Regarding the FWTM, similar changes

were noted for 32 and 16 subsets with the values decreasing and then increase with more iterations. For 8 and 4 subsets the FWTM first decreased but then remain relatively constant.

In the case of the 16mm cylindrical insert the FWHM for 32, 16 and 8 subsets were generally increased with the number of iterations while it decreased for 4 subsets. The FWTM increased with the number iterations for 32 subsets, decreased for 4 subsets and stayed relatively constant for 16 and 8 subsets after an initial increase. In all cases, the poorest resolution was obtained using 4 subsets and a single iteration.

The results agree with those of Miller and Wallis (1992) that an increase in the number of iterations generally improves the spatial resolution.

3.3.2 Noise

The mean counts, the standard deviation of the counts and noise for the 60mm insert cylinder are given in *table 3.2*. Values for different subsets and numbers of iterations (Subset_ iterations) are shown.

The noise for the largest cylinder increased with the number of iterations and is a confirmation of the reported values by Miles et al (1999). However, the noise for 4 subsets fluctuated with the different number of iterations.

Table 3.1: *FWHM and FWTM for the three smaller insert cylinders for different numbers of iteration and subsets.*

Subset_ iterations	32mm Insert		25mm Insert		16mm Insert	
	FWHM (mm)	FWTM (mm)	FWHM (mm)	FWTM (mm)	FWHM (mm)	FWTM (mm)
32_1	27.00	47.53	24.35	40.43	17.98	35.13
32_2	25.92	47.82	23.42	40.28	18.91	36.26
32_5	25.04	47.92	22.74	40.43	19.16	36.60
32_8	24.60	48.36	22.59	40.52	19.21	37.00
32_10	24.40	48.71	22.49	40.57	19.21	37.19
Mean	25.39±1.07	48.07±0.46	23.12±0.78	40.44±0.11	18.89±0.52	36.44±0.81
16_1	25.97	49.69	21.36	43.56	17.98	46.01
16_2	27.39	48.51	22.69	39.94	18.13	37.09
16_5	27.83	48.17	22.25	40.18	19.16	36.06
16_8	27.73	48.17	21.90	40.33	19.40	36.46
16_10	27.73	48.12	21.85	40.47	19.45	36.70
Mean	27.33±0.78	48.53±0.67	22.01±0.49	41.29±1.50	18.83±0.71	38.47±4.23
8_1	26.90	55.17	21.12	45.91	21.66	67.96
8_2	26.71	50.91	20.73	42.58	17.69	63.06
8_5	27.69	48.27	22.25	39.30	18.13	35.72
8_8	28.13	48.07	22.15	39.45	18.91	35.67
8_10	28.57	47.92	22.00	39.54	19.21	35.87
Mean	27.60±0.79	50.07±3.11	21.65±0.68	41.36±2.89	19.12±1.54	47.66±16.39
4_1	34.35	68.55	35.33	48.95	58.85	77.42
4_2	27.29	55.42	21.32	45.82	21.76	68.26
4_5	27.10	49.54	21.07	40.08	17.54	43.12
4_8	27.88	48.31	22.00	39.20	17.74	36.46
4_10	28.18	48.12	22.20	39.25	18.13	35.82
Mean	28.96±3.04	53.99±8.67	24.38±6.14	42.66±4.47	26.80±18.00	52.21±19.32

Table 3.2: *The mean counts, standard deviation of the counts and noise for 60mm cylinder insert.*

60mm insert (Subset_iterations)	Mean counts	Standard deviation	Noise (%)
32_1	2782	183	6.58
32_2	2772	184	6.64
32_5	2760	216	7.83
32_8	2757	233	8.45
32_10	2756	249	9.03
Average	2765	213	7.71
16_1	2826	87	3.08
16_2	2789	110	3.94
16_5	2779	136	4.89
16_8	2775	149	5.37
16_10	2774	162	5.84
Average	2789	129	4.62
8_1	2845	108	3.80
8_2	2833	84	2.97
8_5	2796	96	3.43
8_8	2792	121	4.33
8_10	2791	121	4.34
Average	2811	106	3.77
4_1	2289	125	5.46
4_2	2785	105	3.77
4_5	2776	70	2.52
4_8	2759	82	2.97
4_10	2756	94	3.41
Average	2673	95	3.63

3.4 Discussion

This study showed that an increase in subset number gave better resolution values but increased the noise. Thus, the spatial resolution and noise should not be treated independently. Furthermore, the visual comparison of the images by an experienced observer is essential. Considering all the results, the chosen combination of subset size

and iteration number was 16 subsets with 2 iterations. Although 16 subsets with a single iteration were giving slightly better FWHM values than 16 subsets and 2 iterations, the FWTM values of the latter were better. The noise contribution with these two combinations was almost similar. Therefore, it was decided to use 16 subsets with two iterations for the reconstruction of the patient studies described in Chapter 4.

CHAPTER 4: CLINICAL EVALUATION OF ATTENUATION AND SCATTER CORRECTIONS IN MYOCARDIAL PERFUSION STUDIES

4.1 Introduction	4.1
4.2 Methods.....	4.2
4.2.1 Design of the scanning line source assembly	4.2
4.2.2. Energy settings used for data acquisition.....	4.4
4.2.3 Data acquisition	4.6
4.2.4 Data reconstruction	4.6
4.2.4.1 Transmission data reconstruction	4.7
4.2.4.2 Emission data reconstruction	4.9
4.2.5 Reorientation.....	4.10
4.2.6 Patient data analysis.....	4.10
4.2.7 Attenuation coefficient map analysis.....	4.11
4.3 Results	4.12
4.3.1 Myocardial imaging.....	4.12
4.3.1.1 Group1 (Healthy males)	4.12
4.3.1.2 Group2 (Healthy females)	4.15
4.3.1.3 Group 3 (Male patients)	4.17
4.3.2 Attenuation map analysis.....	4.20
4.4 Discussion	4.22
References	4.24

4.1 Introduction

Single photon emission computed tomography (SPECT) with ^{99m}Tc -MIBI has been widely used to assess myocardial perfusion and provide coronary artery disease (CAD) diagnosis (Wackers, 1996). However, image artefacts caused by non-uniform photon attenuation and Compton scatter of photons are sources of error in the interpretation of images during myocardial SPECT (DePuey and Garcia, 1989). Attenuation of photons from the inferior wall during myocardial perfusion imaging can cause quantitative and qualitative uncertainties in image interpretation (Matsunari et al., 1998). Conventional reconstruction methods for attenuation correction like those of Chang (1978) and Sorenson (1984) are limited in myocardial SPECT imaging because they assume a uniform attenuating medium. New methods of attenuation correction are based on iterative reconstruction techniques, which are commercially available. Often transmission imaging is used to generate patient-specific attenuation maps for attenuation correction of the emission data during iterative reconstruction. In this study, these maps were obtained from a scanning ^{139}Ce line source. The sources of scattered photons in myocardial perfusion studies are the right ventricle and the liver. These affect imaging of the septal wall of the left ventricle and the inferior wall respectively (Tsui et al., 1998). Scatter correction methods must therefore incorporate position-dependent Compton scattering of photons. The method must estimate the contribution of scatter photons to the main energy window of the emission data. The triple energy window (TEW) scatter correction technique proposed by Ogawa et al. (1991) was used as it is quick and easy to use, it is useful in clinical practice (Okada et al., 1999) and it requires no pre-calibration (Ljungberg et al., 1994).

The aim of this part of the study was to evaluate the effect of attenuation and scatter correction in clinical myocardial perfusion imaging.

4.2 Methods

4.2.1 Design of the scanning line source assembly

A scanning line source was used for simultaneous acquisition of emission and transmission data. The line source was mounted on one detector of a Siemens MultiSPECT 2 gamma camera as shown in *figure 4.1* (Naudé, 1998).

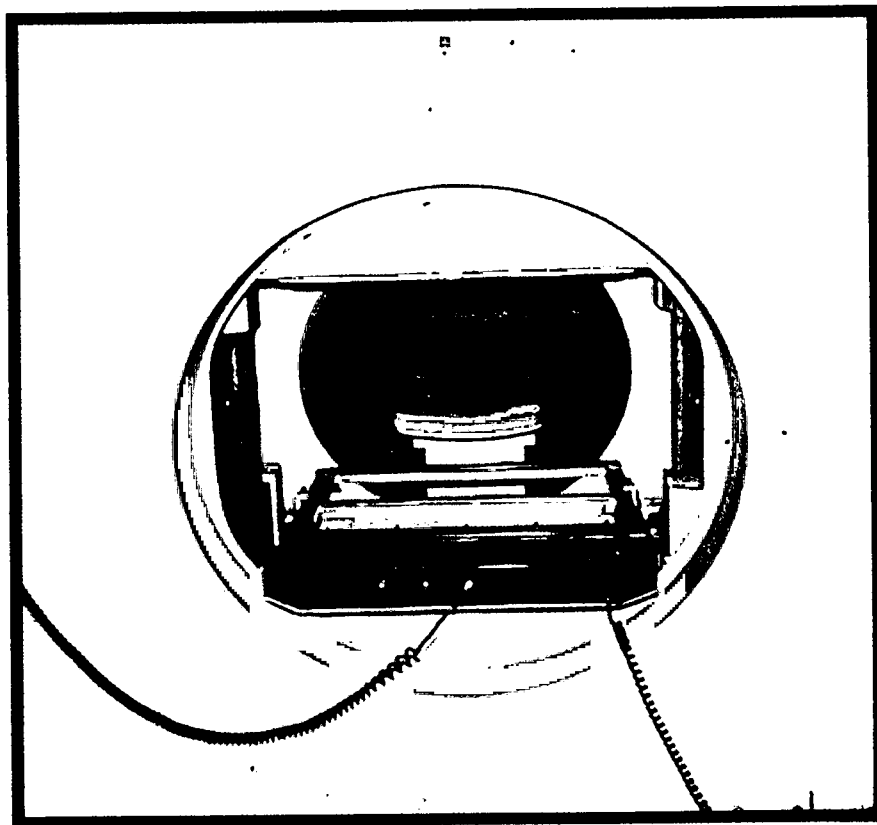


Figure 4.1: *The scanning line source assembly mounted on the dual detector head*

A stepper motor controlled the motion of the scanning line source. The zero position and the end position of the scan path were controlled by micro-switches. In the stop position, the line source was retracted behind lead shielding which limited exposure to the patient, staff and camera detector.

The construction of the line source collimator is shown in *figure 4.2* (Tan et al., 1993). The radionuclide source was sealed in a stainless steel tube with an inner diameter of 2.16mm and an outer diameter of 3.18mm. The line source was collimated with lead, employing a dual slit design to provide narrow beam geometry of the gamma rays while minimising the weight of the device. The back of the line source collimator system was constructed of 11mm lead to ensure nearly complete absorption of photons transmitted in the direction of the detector used as the emission detector (E-detector). The lead collimator was encased in aluminium to ensure rigidity.

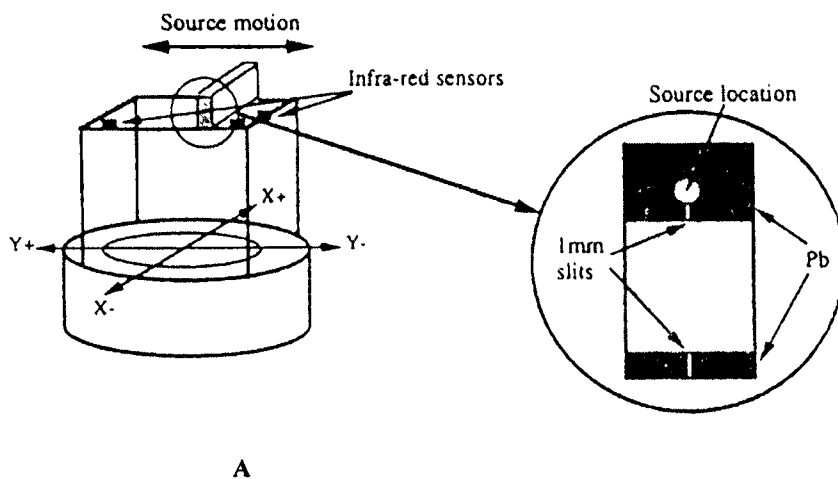


Figure 4.2: **A** shows the source motion and **B** is the cross section of the collimator design indicating the construction of the line source collimator.

The opposing detector was used to acquire both emission and transmission data, referred to as the E-T detector. *Figure 4.3* shows schematically the configuration of the two detectors in the gamma camera system (Naudé, 1998).

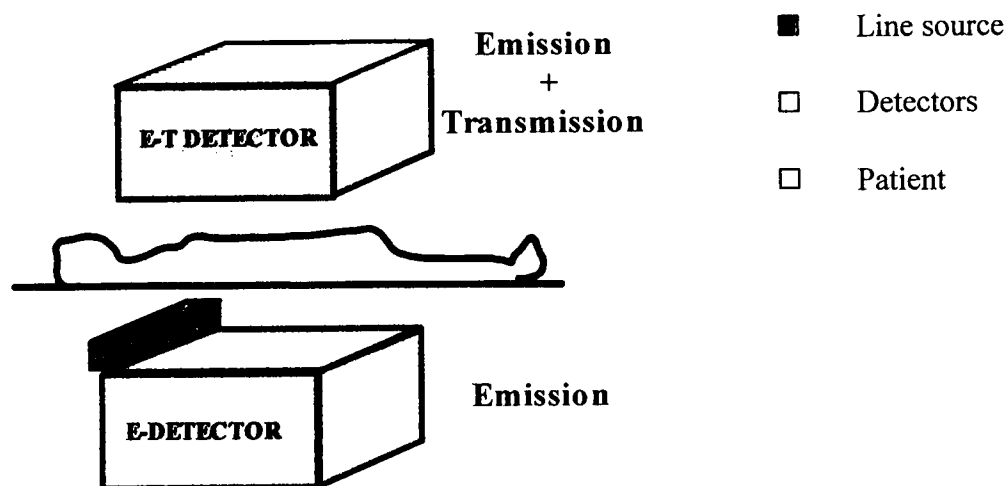


Figure 4.3: A schematic illustration of the two detectors used for data acquisition.

4.2.2. Energy settings used for data acquisition

Myocardial perfusion imaging was performed using ^{99m}Tc as the emission and ^{139}Ce as the transmission source as proposed by Du Raan et al. (2000) and required the following prior settings of the gamma camera for the two opposing detectors. The E-detector was set for a 15% main energy window centred on the 140keV energy peak of ^{99m}Tc and a 3% energy window centred at a -11% offset from 140keV to acquire the scatter data as shown in *figure 4.4* (Naudé, 1998). The E-T detector opposite the scanning line source acquired data using the same main window setting as the E-detector as well as a 15% energy window centred on the 166keV energy peak of ^{139}Ce to acquire transmission data as shown in *figure 4.5* (Naudé, 1998).

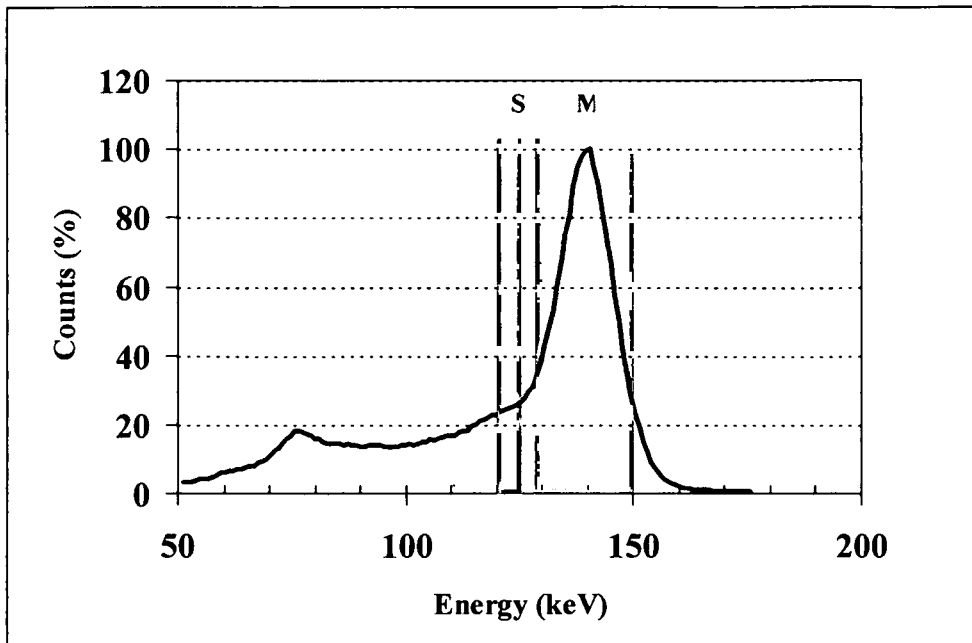


Figure 4.4: Energy spectrum for ^{99m}Tc for the E-detector with S (scatter window) and M (main window).

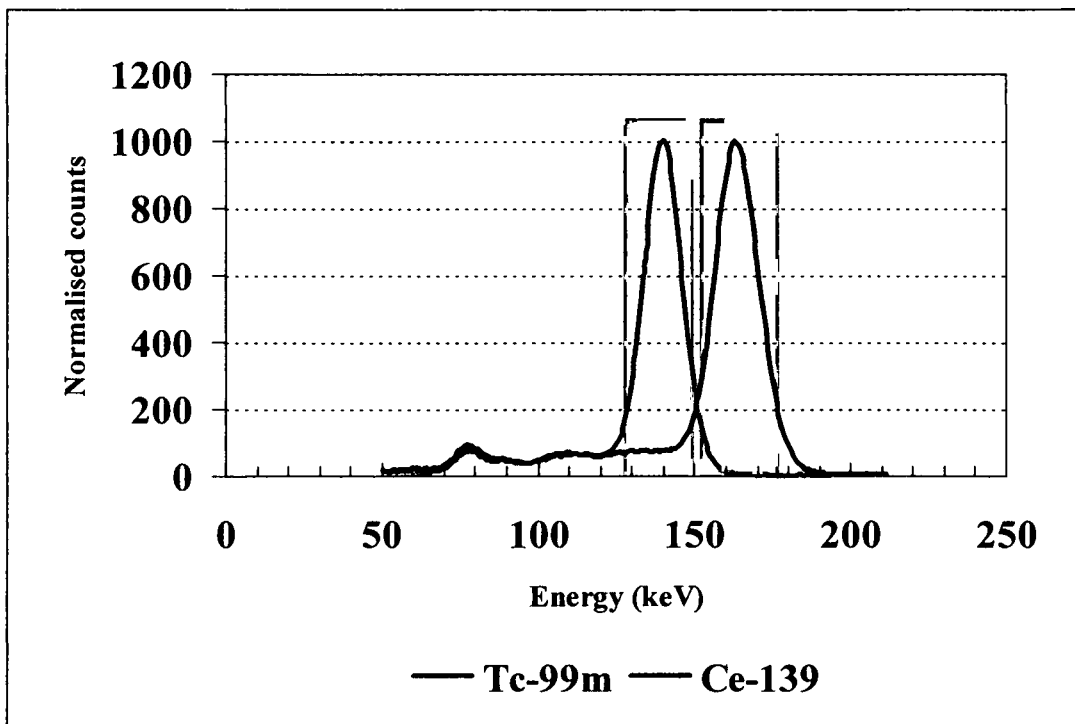


Figure 4.5: The spectra of ^{99m}Tc and ^{139}Ce as obtained with the E-T detector.

4.2.3 Data acquisition

Twelve persons (volunteers and patients) were imaged and divided into three groups. Group 1 consisted of six healthy male volunteers (mean age of 32 years), group 2 of three healthy female volunteers (mean age of 28 years) and group 3 of three male patients (mean age of 60 years) confirmed to have an inferior perfusion defect. Each subject received a dose of 740 MBq of ^{99m}Tc -MIBI at rest, 1 hour prior to data acquisition. The time delay was necessary to ensure extra-cardiac activity excretion which originates mostly from the liver.

Each subject was scanned in the supine position. A post acquisition scanning without the patient, called the "blank scan", was done with the E-T detector. ^{99m}Tc of 37 MBq in a petridish was subsequently imaged for 30 seconds to determine the camera detector sensitivity.

4.2.4 Data reconstruction

Data obtained from the patient and the "blank" scan were reconstructed. In the patient scan, the emission data from the E detector were used because it was not contaminated by transmission data. Transmission data were obtained from the E-T detector, however due to the contamination from the emission data, data acquired in the corresponding projection of the E-detector were subtracted from the E-T data using the following equation:

$$C_T = C_{E-T} - fC_E \quad 4.1$$

C_T is the counts from the transmission window after the subtraction between counts in the E-T and E detectors. C_{E-T} is the counts obtained from the E-T detector in the transmission window. C_E is the counts from the E detector also in the transmission window. The term f

is known as the detector sensitivity factor. The sensitivity factor is due to the masking of the E detector by the line source and different performances of the two detectors. The effect of masking and detector performance can be combined as the inherent sensitivity factor and the dead time as the dynamic sensitivity factor. In this study only the former was measured.

For the determination of the inherent sensitivity factor, a petridish of diameter 65mm containing 8ml of water mixed with 37MBq ^{99m}Tc was used. Three sets of data were acquired i.e. emission data using the E detector with the scanning line source, E detector data without the scanning line source and E-T detector data without the scanning line source. A single projection image of 30seconds duration was obtained in each case. The distance between the radioactive source in the petridish and the detector acquiring the data was kept constant. A 180° camera rotation was required when the acquisition was changed from one detector to the other. The inherent sensitivity correction factor was expressed as the ratio of the counts collected from the emission window of the E-T detector to the counts collected from the emission window of the E detector with the scanning line source.

4.2.4.1 Transmission data reconstruction

For the reconstruction of the attenuation maps, the logarithm of the ratio of the patient transmission data (corrected with *equation 4.1*) to the “ blank” scan transmission data yielded the attenuation coefficient. The transmission projections were converted to line integral projections using the following equation.

$$\mu_{\theta}(i, j) = \ln \left[\frac{N_0(i, j) \times r}{N_{\theta}(i, j)} \right] K \quad 4.2$$

where μ_{θ} is the line integral of the attenuation coefficients of the projection at an angle θ , $N_0(i, j)$ the reference projection "blank scan", $N_{\theta}(i, j)$ is the transmission projection, K is a scaling constant and (i, j) the pixel co-ordinates in the projection matrix.

Due to the higher count-rate in the reference projection (N_0) relative to the transmission projection (N_{θ}), a higher dead time was induced. A region of interest (ROI) of minimum 10 rows and 20 columns in the area of the patient image (N_{θ}) without tissue attenuation for all 64 projections was used to normalise the counts in N_0 to the counts in N_{θ} . A normalisation factor r , equal to the counts in the ROI in the transmission projection divided by the counts in the ROI in the reference projection, was obtained. The counts obtained in the reference projection were multiplied with the normalisation factor r in order to correct for the possible dead-time difference between the reference and transmission projections.

The line integral projections were smoothed using a 3x3 median filter and then reconstructed using the OSEM technique with 16 subsets and 2 iterations to yield the attenuation maps. The ^{139}Ce attenuation maps were converted to attenuation coefficient values for $^{99\text{m}}\text{Tc}$, using the attenuation coefficients measured for water with $^{99\text{m}}\text{Tc}$ and ^{139}Ce line source (Tsui et al., 1989). This is given by:

$$\mu_{\text{Tc}} = (\mu_{\text{Tc}}^{\text{w}} / \mu_{\text{Ce}}^{\text{w}}) \times \mu_{\text{Ce}} \quad 4.3$$

where $\mu_{\text{Tc}}^{\text{w}}$ and $\mu_{\text{Ce}}^{\text{w}}$ are attenuation coefficients experimentally determined in water for $^{99\text{m}}\text{Tc}$ and ^{139}Ce . The attenuation coefficient for $^{99\text{m}}\text{Tc}$, μ_{Tc} , could then be calculated in a medium if the attenuation coefficient for ^{139}Ce , μ_{Ce} , was measured in that medium. Such

a calculation should be accurate for water, soft tissue and lung tissue since the Compton effect dominates at these energies. The attenuation coefficient for bone however, is influenced more by the photoelectric process, therefore in this case such a calculation is not deemed accurate (Welch et al., 1995).

4.2.4.2 Emission data reconstruction

Patient emission data reconstruction was performed in three ways i.e. without any correction, with correction for attenuation only and with correction for both scatter and attenuation.

Emission reconstruction without correction (Nocor)

Emission data from the E detector were used for the reconstruction. The emission data were smoothed using a 3x3 medial filter before reconstruction with the OSEM technique using 16 subsets and 2 iterations. Transverse images of the emission data were obtained over 64 slices.

Emission reconstruction with attenuation correction (Attcor)

The procedure for the reconstruction was similar to the previous paragraph but included the information from the transmission data. During the OSEM reconstruction using 16 subsets and 2 iterations of the smoothed emission image, the attenuation maps obtained from *equation 4.3* were introduced. Transverse images of the emission data corrected for attenuation were obtained.

Emission reconstruction with scatter and attenuation correction (Scat_attcor)

Emission data were corrected for scatter before smoothing and reconstruction. The TEW scatter correction technique (Ogawa et al., 1991) described in *paragraph 2.3.1*, was used to correct for scatter in the emission data. The scatter-corrected image was smoothed before reconstruction using a 3x3 median filter. During the OSEM reconstruction of the

scatter-corrected emission image, the attenuation maps obtained from transmission were incorporated. Transverse images with attenuation and scatter correction were thus obtained.

4.2.5 Reorientation

The axis of the heart does not necessarily align with the body axis. Therefore, reorientation of the heart images was necessary to obtain the short and long axis views perpendicular to the axis of the heart (Haddad et al., 1998). The Siemens Icon Power PC8100 computer was used to select the heart ROI and the reorientation axes. Each set of the emission-reconstructed images was reoriented from the co-ordinate system of the SPECT acquisition to the intrinsic co-ordinate system of the heart. This was followed by interpolation of the tracer activity in the transaxial images (Haddad et al., 1998).

4.2.6 Patient data analysis

Imaging of the heart shows a higher activity distribution of ^{99m}Tc -MIBI in the left ventricle because of the thicker myocardial muscle cells in that region of the heart.

The left ventricle image was divided into three divisions - basal, medial and apical, as shown in *figure 4.6A*. All reconstructed slices obtained from these divisions were processed for counts quantification using a second derivative edge detection method so that the area of the image containing myocardial muscle of the ventricle was identified. Each slice was subdivided into anterior, lateral, inferior and septal regions as shown in *figure 4.6B*. The counts and the number of pixels were calculated in each section. Average count density and numbers of pixels were calculated for only two slices selected in each division. The image sets were then superimposed to obtain "Bull's eye"(BE)

images that eventually consisted of 12 regions, as shown in *figure 4.6C*. The counts in the 12 regions of the three image sets (nocor, attcor and scat_attcor) were normalised to the maximum value of all three sets.

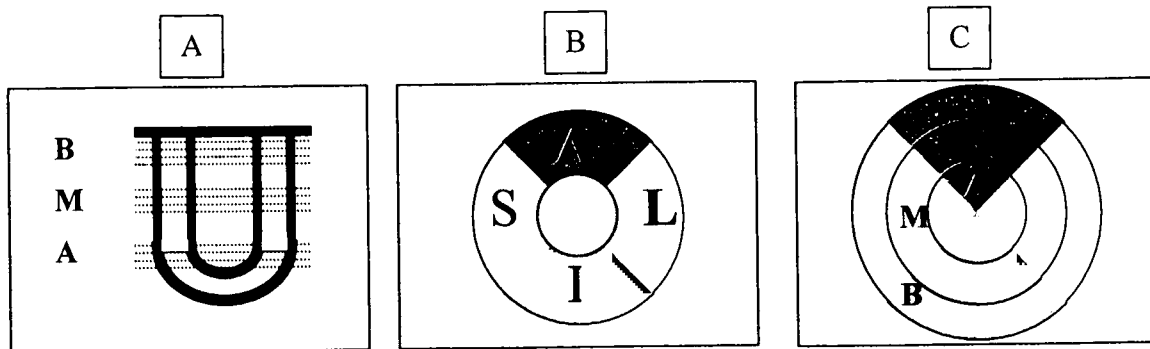


Figure 4.6 *Data presentation of the patient data*

The final data were averaged separately for the different groups. The ratio of counts in the inferior wall to the counts in the anterior wall was compared to evaluate the effect of attenuation and scatter correction.

Bull's eye results were presented as the average normalised counts \pm standard deviation for the three groups of subjects.

4.2.7 Attenuation coefficient map analysis

The accuracy of the value of the attenuation coefficient in the heart was determined by calculating the pixel counts over the heart area of the subjects. An average count of three slices of attenuation maps in the ROI over the heart, which excluded the lung activity, was used for this study. Attenuation coefficient accuracy was expressed as the average attenuation map value \pm standard deviation, and was compared to values obtained from the literature (ICRU, 1989).

A signal-to-noise (S/N) ratio was calculated to evaluate the spatial variation in the attenuation maps. It was defined according to the integral uniformity as recommended by NEMA (1994), and given by:

$$S / N = 100 * \left[\frac{MAX - MIN}{MAX + MIN} \right] \quad 4.4$$

MAX is the maximum pixel count and MIN the minimum pixel count within the ROI selected.

Mean attenuation coefficient values were calculated from three slices in the region of the heart for the ^{139}Ce and for the attenuation maps converted to $^{99\text{m}}\text{Tc}$. Average S/N ratios for these attenuation maps were compared.

4.3 Results

4.3.1 Myocardial imaging

The results of the three groups will be discussed separately.

4.3.1.1 Group1 (Healthy males)

The average BE plots for the subjects in this group is shown in *figure 4.7*. The values for the uncorrected data (*figure 4.7a*) varied from a maximum of 0.22 in apical-lateral and apical-septal regions to minimum of 0.14 in the basal-septal region representing a difference of 36%. Attenuation correction improved these values as shown in *figure 4.7b*. The difference between the apical-lateral segment (0.82) and basal-septal segment (0.72) decreased to 12% and decreased to 15% between apical-septal segment (0.85) and basal-septal region (0.72) (it was 36%). The minimum still was found in the apical anterior region (0.72) while the maximum was found in the medial-inferior region (0.98).

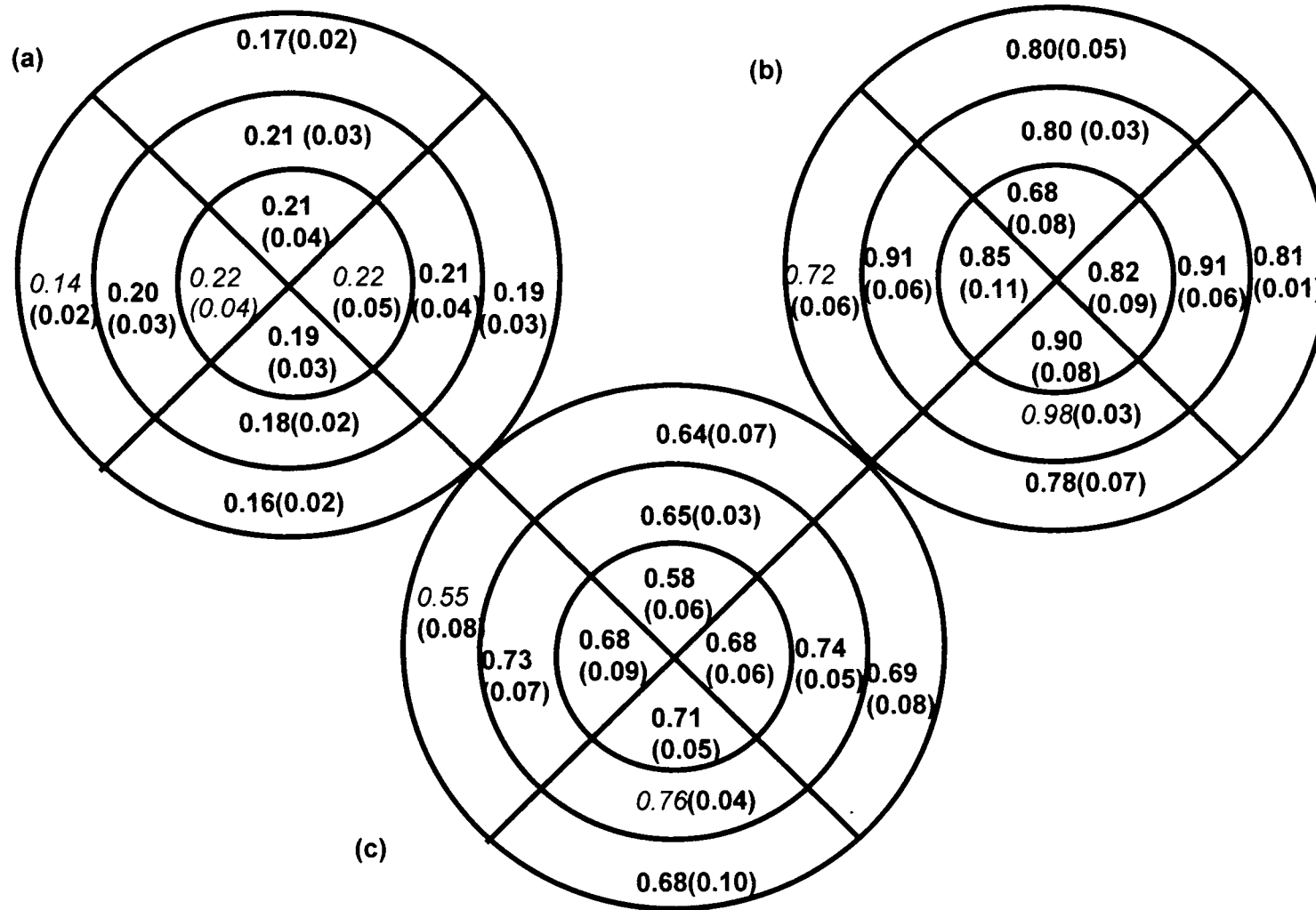


Fig.4.7: Average normalised counts for the HEALTHY MALES, with standard deviations. (a) uncorrected data (b) attenuation corrected data (c) attenuation and scatter corrected data

The difference between the minimum and maximum values was 27% (Values shown in *italics*).

Additional scatter correction resulted in lower count density compared to when only attenuation correction was applied (*figure 4.7c*). A maximum of 0.76 was found in the medial inferior region and a minimum of 0.55 in the basal-septal region. This presented a difference of 28%.

The average count ratio of the inferior/ anterior regions (Inf/ ant) and septal/ lateral regions (Sept/ lat) for the medial section of the myocardium are indicated in *table 4.1*. The average ratios were 0.90 and 0.88 before any correction respectively. Attenuation correction improved the count ratios to 1.17 and 0.97, however the inclusion of scatter correction slightly reduced the count ratio to 1.14 and 0.92.

Table 4.1: *The count ratios Inf/ ant and Sept/ lat for the medial section of the myocardium for the healthy males.*

Inf/ant	Volunteer 1	Volunteer 2	Volunteer 3	Volunteer 4	Volunteer 5	Volunteer 6	Average
nocor	0.98	0.90	0.90	0.82	0.84	0.95	0.90±0.06
attcor	1.26	1.16	1.08	1.08	1.18	1.24	1.17±0.08
Scat_attcor	1.25	1.12	1.03	1.12	1.14	1.20	1.14±0.08

Sept/lat	Volunteer 1	Volunteer 2	Volunteer 3	Volunteer 4	Volunteer 5	Volunteer 6	Average
Nocor	0.88	0.85	0.92	0.86	0.94	0.85	0.88±0.04
Attcor	1.02	0.93	1.11	0.92	0.90	0.95	0.97±0.08
Scat_attcor	0.93	0.91	1.04	0.88	0.89	0.89	0.92±0.06

An example of medial short axis slice of one subject in this group is shown in *figure 4.8*.

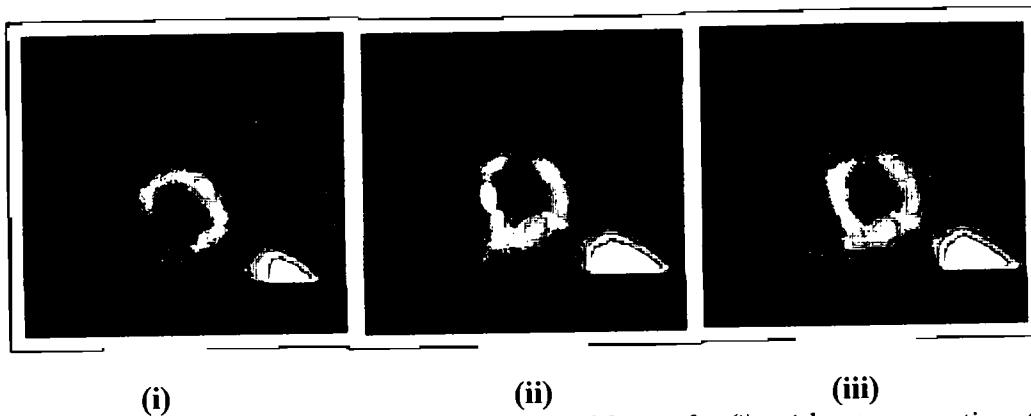


Figure 4.8: *Medial short axis slice of a healthy male (i) without correction (ii) with attenuation correction and (iii) with scatter and attenuation correction*

4.3.1.2 Group2 (Healthy females)

Figure 4.9 shows the average BE plots for the subjects in this group. The values for the uncorrected data (*figure 4.9a*) varied from a maximum of 0.22 in apical-septal region to a minimum of 0.14 in the basal-septal region representing a difference of 36%. Attenuation correction improved these values (*figure 4.9b*). The difference between the apical-septal 0.88 and basal-septal 0.72 regions decreased to 18%. The minimum was still in the basal-septal region 0.72 while the maximum was found in the medial-inferior. The difference between the minimum and maximum values was 27% (values shown in *italics*).

Additional scatter correction resulted in lower values compared to when attenuation correction was only applied (*figure 4.9c*). A maximum of 0.80 was found in the medial-inferior region and a minimum of 0.58 in the basal-septal region. This presented a difference of 28%. These results were similar to that obtained for the healthy male group.

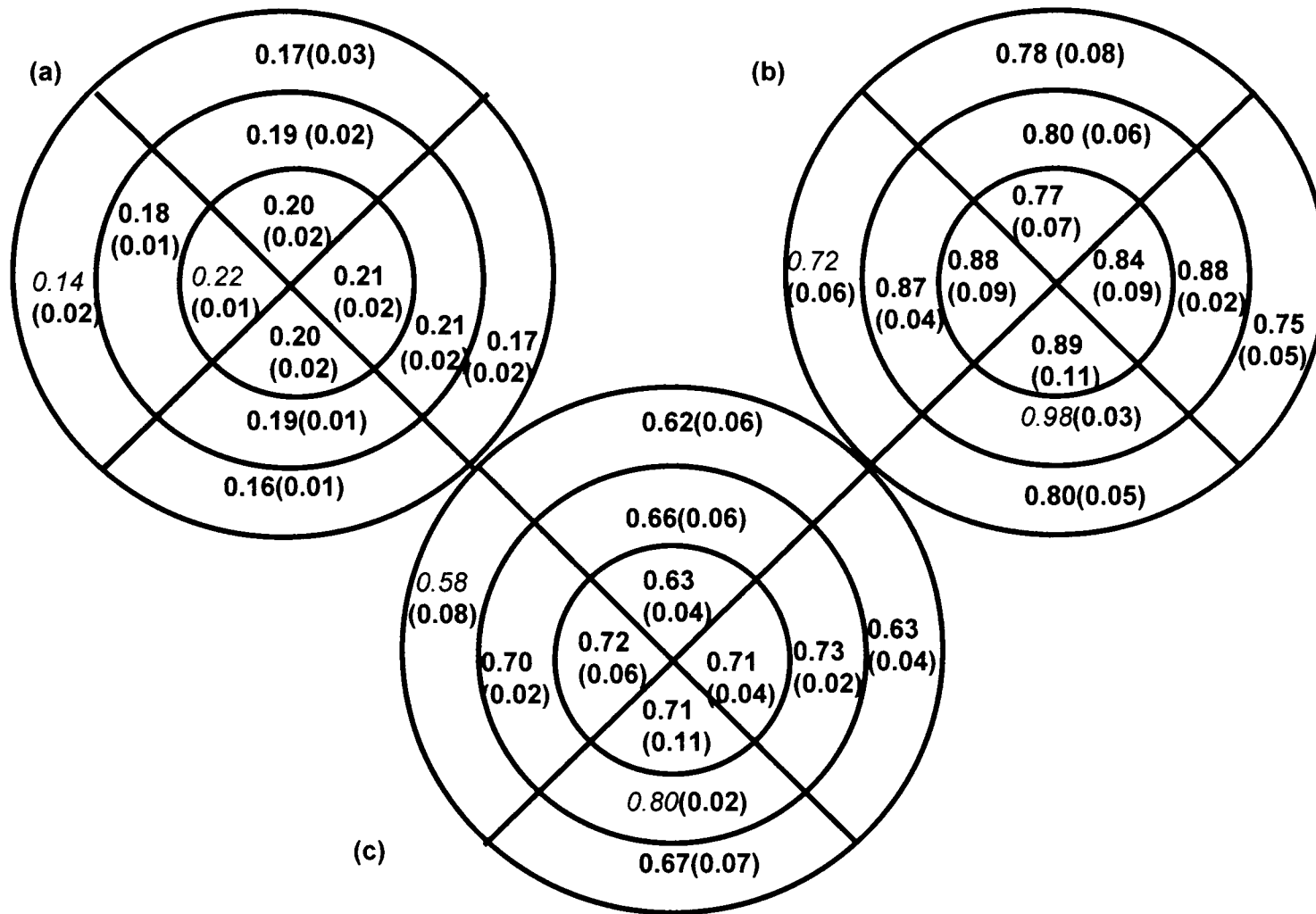


Fig.4.9: Average normalised counts for the HEALTHY FEMALES, with standard deviations. (a) uncorrected data (b) attenuation corrected data (c) attenuation and scatter corrected data

The average count ratio of the Inf/ ant and Sept/ lat for the medial part was 0.98 and 0.92 before any correction respectively (*table 4.2*). Attenuation improved the count ratio to 1.14 and 1.00 respectively, however the scatter correction did not change the Inf/ ant ratio of 1.14 but the Sept/ lat ratios was slightly reduced from 1.00 to 0.97.

Table 4.2: *The count ratios Inf/ ant and Sept/ lat for the medial section of the myocardial for the healthy females.*

Inf/ant	Volunteer 1	Volunteer 2	Volunteer 3	Average
Nocor	0.95	1.02	0.97	0.98±0.04
Attcor	1.20	1.17	1.05	1.14±0.08
Scat_attcor	1.16	1.16	1.11	1.14±0.03

Sept/lat	Volunteer 1	Volunteer 2	Volunteer 3	Average
Nocor	0.85	0.94	0.97	0.92±0.06
Attcor	0.95	1.04	1.02	1.00±0.05
Scat_attcor	0.91	0.99	1.00	0.97±0.05

An example of a medial short axis slice of a subject in this group is shown in *figure 4.10*

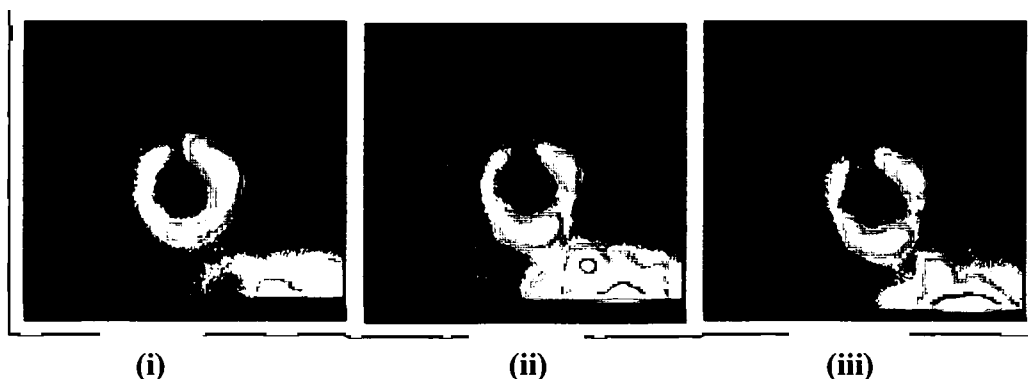


Figure 4.10: *Medial short axis slice of a healthy female (i) without correction (ii) with attenuation correction and (iii) with scatter and attenuation correction*

4.3.1.3 Group 3 (Male patients)

In this group the average BE plots are shown in *figure 4.11*. The values for the uncorrected data in *figure 4.11a* varied from a maximum of 0.16 in apical-anterior, medial-anterior, apical-septal, medial-lateral, and apical-lateral regions to a minimum of

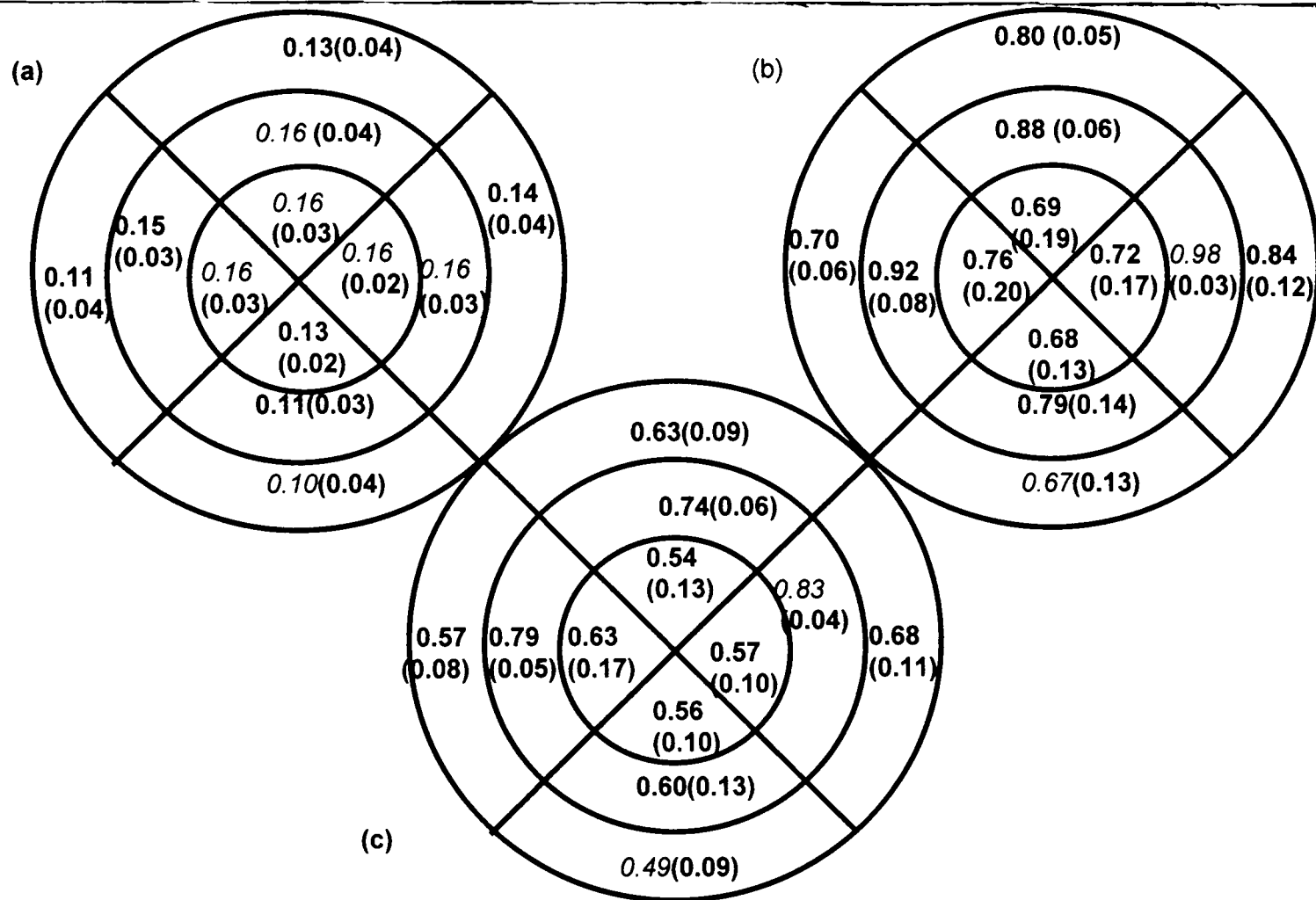


Fig.4.11: Average normalised counts for the UNHEALTHY MALE PATIENTS, with standard deviations. (a) uncorrected data (b) attenuation corrected data (c) attenuation and scatter corrected data.

0.10 in the basal inferior region representing a difference of 38%. Attenuation correction improved these values (*figure 4.11b*). The difference between the five above-mentioned regions (average of 0.81) and basal-inferior region 0.67 decreased to 17%. The minimum was found in the basal-inferior region 0.67 while the maximum was found in the medial-lateral region (0.98). The difference between the minimum and maximum values was 32% (values shown in *italics*). This is expected since the patients had a defect in the inferior region.

Additional scatter correction resulted in lower values compared to when only attenuation correction was applied (*figure 4.11c*). The relative distribution of the values was the same as previously. A maximum of 0.83 was found in the medial-lateral region and a minimum of 0.49 in the basal- inferior region. This presented a difference of 41%, indicating the inferior defect clearly.

The average Inf/ ant and Sept/ lat count ratio for the medial part was 0.77 and 0.92 before any correction respectively (*table 4.3*). Attenuation correction improved the count ratio to 0.91 and 0.95 respectively, however the inclusion of scatter correction reduced the Inf/ ant ratio value to 0.86 while the Sept/ lat remained almost constant.

Table 4.3: *Count ratios Inf/ant and Sept/ lat for the medial section of the myocardium for the male patients group.*

Inf/ant	Volunteer 1	Volunteer 2	Volunteer 3	Average
Nocor	0.85	0.79	0.68	0.77±0.09
Attcor	0.87	1.06	0.79	0.91±0.14
Scat_attcor	0.85	0.95	0.79	0.86±0.08

Sept/lat	Volunteer 1	Volunteer 2	Volunteer 3	Average
Nocor	0.92	0.92	0.92	0.92±0.00
Attcor	0.82	1.00	1.02	0.95±0.11
Scat_attcor	0.82	0.98	1.09	0.96±0.14

An example of a medial short axis slice of one patient in this group is shown in *figure 4.12*.

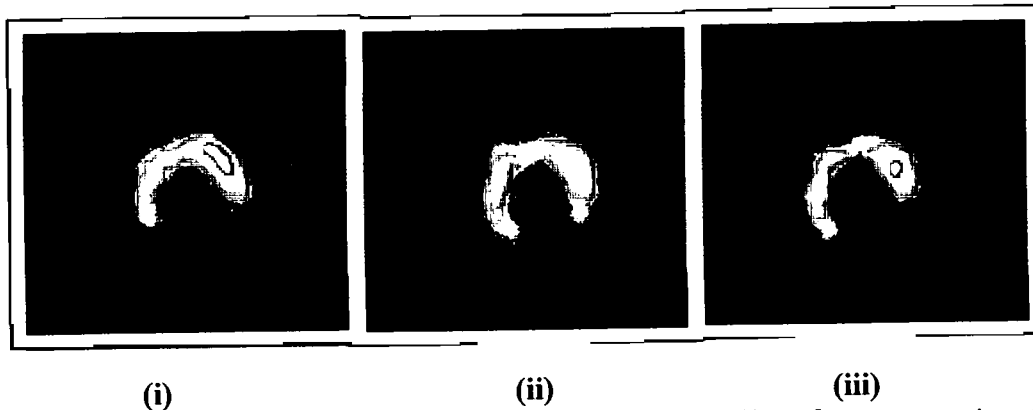


Figure 4.12: Medial short axis slice of a male patients (i) without correction (ii) with attenuation correction and (iii) with scatter and attenuation correction

4.3.2 Attenuation map analysis

The average measured attenuation coefficients for 12 subjects in the region of the heart were determined and are listed in *table 4.4*. An average value of $0.0137 \pm 0.00017\text{mm}^{-1}$ was obtained for ^{139}Ce . This underestimated the value of 0.0150mm^{-1} obtained from ICRU (1989) by 9%. An average S/N ratio of $16.81 \pm 5.9\%$ was obtained for the ^{139}Ce attenuation maps as shown in *table 4.5*.

The converted attenuation coefficient values from ^{139}Ce to $^{99\text{m}}\text{Tc}$ were also compared to the ICRU (1989) value. An average value of $0.0159 \pm 0.00019\text{mm}^{-1}$ was obtained. This overestimated the ICRU (1989) value of 0.0157mm^{-1} by 1%. An average S/N ratio of $16.27 \pm 5.6\%$ was obtained for the converted attenuation maps.

Table 4.4: Illustration of attenuation coefficient for ^{139}Ce and converted value to $^{99\text{m}}\text{Tc}$ compared to the reference value.

Attenuation coefficients(mm^{-1})				
Subjects	^{139}Ce		$^{99\text{m}}\text{Tc}$	
	Measured	Reference	Converted	Reference
1	0.0147 ± 0.00010		0.0171 ± 0.00012	
2	0.0134 ± 0.00014		0.0155 ± 0.00016	
3	0.0134 ± 0.00001		0.0156 ± 0.00002	
4	0.0136 ± 0.00014		0.0158 ± 0.00017	
5	0.0146 ± 0.00060		0.0169 ± 0.00070	
6	0.0141 ± 0.00046		0.0163 ± 0.00054	
7	0.0131 ± 0.00007		0.0151 ± 0.00009	
8	0.0136 ± 0.00024		0.0158 ± 0.00028	
9	0.0136 ± 0.00019		0.0158 ± 0.00021	
10	0.0135 ± 0.00024		0.0156 ± 0.00028	
11	0.0135 ± 0.00020		0.0157 ± 0.00023	
12	0.0135 ± 0.00031		0.0157 ± 0.00035	
Average \pm std	0.0137 ± 0.0002	0.0150	0.0159 ± 0.0002	0.0157

Table 4.5: A comparison of the signal- to- noise (S/N) ratios for the measured and converted attenuation coefficient values

Subject	S/N (%)	
	^{139}Ce Measured	$^{99\text{m}}\text{Tc}$ Converted
1	16.27	16.27
2	9.50	9.48
3	16.59	16.59
4	8.14	8.14
5	27.28	27.28
6	18.30	16.02
7	20.31	19.95
8	22.62	22.62
9	24.16	20.31
10	12.73	12.73
11	12.03	12.03
12	13.80	13.80
Average	16.81 ± 5.90	16.27 ± 5.60

4.4 Discussion

In this study the clinical utility of attenuation and scatter correction of SPECT myocardial perfusion studies was evaluated in normal persons as well as patients with a confirmed inferior perfusion defect. The effect of attenuation and scatter correction was evaluated by (a) quantitating the regional myocardial uptake and (b) comparing the count ratios of the inferior to anterior and septal to lateral myocardial regions. The regional myocardial uptake as expressed in the different BE plots showed a definite pattern for all three groups. The uptake in all regions was increased compared to the uncorrected values when only attenuation correction was done. When scatter correction was added to the latter a decrease in the uptake values was noted. In all the groups lower perfusion values were found in the anterior segment of the myocardium following attenuation correction only and combined scatter and attenuation correction. This observation could be attributed to an overcorrection of the inferior wall and could be perceived as an artefactual decrease of myocardium uptake in the anterior wall. This apparent overcorrection can also be the result of no correction or an undercorrection for scattered counts in this region originating from the liver. The scattered counts will contribute to the inferior wall and higher perfusion values will be obtained in this region.

The Inf/ ant ratio in Group 1 decreased from 1.17 for attenuation corrected data to 1.14 for data corrected for scatter and attenuation. This is an indication that the counts in the inferior wall decrease relative to counts in the anterior after applying the scatter correction. The average ratio remained stable (1.14) for Group 2, however a decrease in the Inf/ant ratio could be seen in 2 of the 3 volunteers. It is very important to note that in the patient group (Group 3) the Inf/ ant count ratio remained smaller than unity. This is a

clear indication that the existing inferior perfusion defect in this patient group was not artefactually eliminated with attenuation and scatter correction.

The average attenuation coefficient value obtained with the ^{139}Ce scan was lower than that given by the ICRU (0.0137mm^{-1} vs 0.0150mm^{-1}). However, after conversion of the values to $^{99\text{m}}\text{Tc}$ energy values, the mean attenuation coefficient value was almost similar to the ICRU value (0.0159mm^{-1} vs 0.0157mm^{-1}). This confirms that an acceptable transmission correction could be performed. The latter attenuation coefficients furthermore yielded reconstructed images that were similar regarding noise propagation to that obtained with the ^{139}Ce scan (16.27 vs. 16.81).

The study showed that the scatter and attenuation correction techniques still need further evaluation before they can be applied clinically. The contribution of the scattered counts from the liver to the inferior wall needs to be investigated thoroughly. The accuracy of the scatter correction in this specific application should also be evaluated.

References

- Chang LT (1978). A method for attenuation correction in radionuclide computed tomography. *IEEE Trans Nucl Sci*; NS-25: pp638 – 643.
- De Puey EG, Garcia EV (1989). Optimal specificity of thallium ^{201}Tl SPECT through recognition of imaging artefact, *J Nucl Med*; 30: pp441–9.
- Du Raan H, du Toit PD, van Aswegen A, MG Lötter, Herbst CP, van der Walt TN, Otto AC (2000). Implementation of a Tc-99m and Ce-139 scanning line source for attenuation correction in SPECT using dual opposing detector scintillation system. *Med Phys*; 27: pp 1523 – 1534.
- Haddad M, Porenta G (1998). Impact of reorientation algorithms on quantitative myocardium SPECT perfusion imaging. *J Nucl Med*; 39: pp1864 – 1869.
- Ljungberg M, King MA, Hademenos GJ, Strand S-E (1994). Comparison of four scatter correction methods using Monte Carlo simulated source distributions. *J Nucl Med*; 35: pp143 – 151.
- Matsunari I, Boning G, Ziegler S I, Kosa I, Nekolla SG, Ficaro EP, Schwaiger M (1998). Effects of misalignment between transmission and emission scans on attenuation corrected cardiac SPECT. *J Nucl Med*; 39, pp411 – 416.
- Naudé H (1998). Scatter and attenuation correction techniques for absolute quantification of radionuclide distributions with SPECT. *PhD Thesis*, UOVS, Bloemfontein.
- Ogawa K, Harata Y, Ichihara T, Kubo A, Hashimoto S (1991). A practical method for position-dependent Compton-scatter correction in single photon emission CT. *IEEE Trans Med Imag*; 10: pp408 – 412.
- Okada J, Imai Y, Tamada H, Kawashiro O, Yui N, Togawa T, Kinoshita F, Ito H (1999). ^{67}Ga planar imaging with a low-energy collimator and scatter correction using the triple energy method. *Nucl Med Comm*; 20: pp647 – 657.
- Performance Measurements of Scintillation Cameras. NEMA standard publication NU1, 1994.
- Sorenson JA (1984). Quantitative measurement of radiation *in vivo* by whole body counting, in Hine GH, Sorenson JA (eds): *Instruments in Nuclear Medicine*, vol 2. New York, NY, Academic, pp 311-349.
- Tan P, Bailey DL, Meikle SR, Eberl S, Fulton RR, Hutton BF (1993). A scanning line source for simultaneous emission and transmission measurements in SPECT. *J Nucl Med*; 34: pp1752 – 1760.

- ICRU Report 44 (1989). Tissue substitutes in radiation dosimetry and measurement.
- Tsui BMW, Gullberg GT, Edgerton ER, Ballard JG, Perry JR, McCartney WH, Berg J (1989). Correction of nonuniform attenuation in cardiac SPECT imaging. *J Nucl Med*; 30: pp497 – 507.
- Tsui BMW, Frey EC, LaCroix KJ, Lalush DS, McCartney WH, King MA, Gullberg GT (1998). Quantitative myocardial perfusion SPECT. *J Nucl Med*; 5: pp507 – 522.
- Wackers FJ (1996). Myocardial perfusion imaging. In: Sandler MP, Coleman RE, editor. *Diagnostic Nuclear Medicine*. 3rd ed. Baltimore; Williams and Wilkins: pp443-561.
- Welch A, Gullberg GT, Christian PE, Tsui BMW (1995). An investigation of dual-energy transmission measurements in simultaneous transmission and emission imaging. *IEEE Trans Nucl Sci*; 42: pp2331 – 2338.

References

- Hutton BF, Lau YH (1997). How critical is subset balance for OSEM reconstruction in myocardial SPECT? *J Nucl Med*; 38, Suppl, p57P.
- Miles J, Cullom J, Case A (1999). An introduction to attenuation correction. *J Nucl Cardiol*; 6: pp449 – 457.
- Miller TR, Wallis JW (1992). Clinically important characteristics of maximum-likelihood reconstruction. *J Nucl Med*; 33: pp1678 – 1684.
- Naudé H (1998). Scatter and attenuation correction techniques for absolute quantification of radionuclide distributions with SPECT. *PhD Thesis*, UOVS, Bloemfontein
- Sorenson JA, Phelps ME (1987). Image quality in Nuclear Medicine. In: *Physics in Nuclear Medicine*, 2nd edition; WB Saunders Company, Philadelphia, pp362-366.
- Tsui BMW, Gullberg GT, Edgerton ER, Ballard JG, Perry JR, McCartney WH, Berg J (1989). Correction of nonuniform attenuation in cardiac SPECT imaging. *J Nucl Med*; 30: pp497 – 507.

Summary

The purpose of this study was firstly to evaluate the selection of reconstruction parameters (i.e. the number of subsets and the number of iterations) based on phantom studies. The second aim was to evaluate the effect of the non-uniform attenuation and scatter correction on myocardial perfusion studies performed on healthy volunteers as well as patients with proven inferior wall perfusion defects.

The quality of the images from the phantom studies showed that 16 subsets with 2 iterations gave the best results if considering image noise and image resolution. These number of subsets and iterations were therefore used as reconstruction parameters in the patient studies

The application of an attenuation correction to the emission data required that attenuation coefficient maps of the subjects were obtained from transmission images. ^{139}Ce was chosen as the transmission source and used in conjunction with $^{99\text{m}}\text{Tc}$ as the emission source. The emission data were corrected for scatter according to the triple energy window method.

In the healthy male and female volunteers, the attenuation and scatter corrected myocardial SPECT images showed an improvement in the homogeneity of the counts distribution compared to the uncorrected images. The counts distribution in the inferior region improved after the attenuation correction was applied, however it exceeded the counts in the anterior region. After applying a scatter as well as an attenuation correction to the emission data, the counts in the inferior region of the myocardium were slightly reduced. This was a result of the scatter correction

eliminating scattered counts in the inferior region originating mainly from the liver. The apparent lower counts in the anterior region could be a result of too little compensation for scatter in the inferior wall, and needs to be investigated further.

The defects in the three unhealthy patients, were not obscured after applying the scatter and attenuation correction to the emission data. The correction technique did not introduce false negative results in these patients.

The application of scatter and attenuation correction techniques shows promising results for the interpretation of myocardial perfusion studies. These correction algorithms however need to be investigated thoroughly before being used in the routine clinical practice to avoid the introduction of artefacts.

Keywords: SPECT; nuclear cardiology; attenuation correction; scatter correction; transmission imaging; scanning line source; iterative reconstruction; myocardial perfusion; coronary artery disease; ^{99m}Tc MIBI.

i 152 216 72

U.O.V.S. BIBLIOTEK